Stress drops and earthquake triggering drop sequences in the simplest pressure-sensitive ideal elasto-plastic media: Implications for earthquake cycles

Yury Alkhimenkov¹, Lyudmila Khakimova^{2,3}, and Yury Podladchikov^{2,3}

Correspondence: Yury Alkhimenkov (yalkhime@mit.edu; yalkhime@gmail.com)

Abstract. This study explores stress drops and earthquake triggering within the simplest sequences in the simplest pressure-sensitive elasto-plastic media using two-dimensional simulations, emphasizing the critical role of temporal and spatial resolutions resolution in accurately capturing stress evolution and strain fields localization during seismic cycles. Our analysis reveals that stress drops, triggered by plastic deformation once local stresses reach the yield eriteria, reflect criterion—resemble fault rupture mechanics, where accumulated strain energy is released suddenly, simulating earthquake suddenly released, simulating earthquake-like behavior. Finer temporal and spatial discretization leads to sharper stress drops and lower minimum stress values, while finer spatial grids provide more detailed representations of strain localization and stress redistribution. Our analysis reveals that displacement. Displacement accumulates gradually during interseismic periods and intensifies during major stress drops, reflecting capturing key features of natural earthquake cycles.

The histogram of stress drop amplitudes shows exhibits a non-Gaussian distribution, characterized by a broad peak with long tails on both sides, where small stress drops are more frequent, but large stress drops still occur with significant probability.

This "solid turbulence" behavior suggests that stress is redistributed across spatial and temporal scales, with implications for understanding the variability of stress drop magnitudes.

Our results demonstrate that high-resolution elasto-plastic models ean reproduce key can reproduce essential features of earthquake triggering nucleation and stress drop behavior without relying on complex frictional friction laws or velocity-dependent weakening mechanisms. These findings emphasize the necessity of incorporating plasticity into models of fault slip models to better understand the mechanisms governing of fault weakening and rupture. Furthermore, our work suggests that extending these models to three-dimensional fault systems and accounting for incorporating material heterogeneity and fluid interactions could provide offer deeper insights into seismic hazard assessment and earthquake mechanics.

10

¹Department of Civil and Environmental Engineering, Massachusetts Institute of Technology, Cambridge, MA 02139, USA

²Institute of Earth Sciences, University of Lausanne, Switzerland

³Faculty of Mechanics and Mathematics, Lomonosov Moscow State University, Moscow 119991, Russia

1 Introduction

30

35

50

Understanding earthquake triggering remains a significant challenge in geophysics, as it directly influences our ability to predict and mitigate seismic hazards. Earthquake nucleation is often conceptualized through the study of sliding behavior along fault surfaces, with models traditionally describing the interseismic period as one of near-elastic deformation in the surrounding crust, interrupted by phases of anelastic slip that eventually result in seismic rupture (Pranger et al., 2022). Such models typically rely on phenomenological rate- and state-dependent friction laws (Dieterich, 1978, 1979; Ruina, 1983), which have been highly successful in describing various aspects of the seismic cycle. However, these friction-based models may overlook critical physical processes that govern the transition from aseismic slip to seismic rupture, particularly when plastic deformation and off-fault processes are involved.

Numerical modeling of elasto-plastic behavior strain localization in pressure-sensetive geo-materials has a long history, with early contributions from Cundall (1989, 1990); Poliakov et al. (1993, 1994); Poliakov and Herrmann (1994). Regularization of strain localization thickness was addressed by Duretz et al. (2019) and de Borst and Duretz (2020). A single-phase (visco)-hypoelastic-perfectly plastic medium was modeled in both 2D and 3D domains by Alkhimenkov et al. (2024b), while compaction-driven fluid flow and shear bands in porous media were numerically modeled in 3D by Alkhimenkov et al. (2024a).

One of the first computational earthquake dynamics models with slip-weakening rupture simulations was introduced by Andrews (1976). Recent studies have suggested that plasticity plays a crucial role in the triggering of earthquakes, particularly through off-fault plasticity mechanisms (e.g., Andrews (2005)). Off-fault plasticity refers to the deformation that occurs away from the main fault plane and can significantly influence the dynamics of rupture propagation. Ma (2008); Ma and Andrews (2010) conducted some of the earliest studies on dynamic rupture with plasticity. Previous works have explored the effects of off-fault plasticity in two-dimensional (2-D) in-plane dynamic rupture simulations (Templeton and Rice, 2008; Kaneko and Fialko, 2011; Gabriel et al., 2013; Tong and Lavier, 2018; Allison and Dunham, 2018). For instance, Dal Zilio et al. (2022) presented a 2-D thermomechanical computational framework for simulating earthquake sequences in a nonlinear visco-elastoplastic compressible medium, highlighting the importance of including viscoelastic and plastic behavior in realistic models. Other studies highlighting the importance of plasticity in earthquake physics modeling include Erickson et al. (2017), Preuss et al. (2020), and Simpson (2023).

In addition to 2-D studies, three-dimensional (3-D) dynamic rupture simulations incorporating off-fault plasticity have provided deeper insights into the complexity of earthquake mechanics (Wollherr et al., 2018). Another significant advancement was made by Uphoff et al. (2023), who utilized a discontinuous Galerkin method to model earthquake sequences and aseismic slip on multiple faults, demonstrating the versatility of numerical approaches in capturing the nuances of seismic phenomena.

The role of plasticity in earthquake triggering has also been emphasized in laboratory experiments. Studies have shown that plastic deformation can precede seismic slip, indicating that the onset of plastic yielding may be a precursor to earthquake initiation (Johnson et al., 2008; Scuderi et al., 2016). These experimental findings support the incorporation of plasticity in numerical models to enhance the understanding of the triggering process.

Despite these advancements, there remains a need for simplified models that can effectively capture the essential features of earthquake triggering and stress drops while being computationally efficient. The simplest elasto-plastic models offer a promising avenue for such investigations. By focusing on basic physical principles, these models can provide insights into the fundamental mechanisms of earthquake triggering, such as the role of stress accumulation and release, the interaction between elastic and plastic deformation, and the influence of material heterogeneity on seismic behavior.

In this study, we employ a two-dimensional elasto-plastic model to investigate stress drops and earthquake triggering. The friction coefficient is assumed to be constant in all simulations, with no hardening or softening, which corresponds to an ideal plasticity model. We conduct a series of numerical simulations to explore the effects of temporal and spatial resolutions on the accuracy of stress and strain predictions. Our goal is to understand how these resolutions impact the modeled behavior of stress evolution, strain accumulation, and the nucleation of seismic events. Our approach involves detailed convergence tests for temporal and spatial discretizations, analysis of stress drop sequences, and examination of interseismic periods. We also investigate the initial wave field patterns during earthquake nucleation to gain insights into the complex interplay between quasi-static and elasto-dynamic mechanics. Through this comprehensive study, we aim to highlight the critical role of high-resolution modeling in capturing the intricate dynamics of earthquake triggering and stress drops, providing a foundation for future research and practical applications in seismic hazard assessment.

The novelty of the present study is highlighted by the following contributions:

- 1. We utilize employ the simplest pressure-sensitive ideal plasticity model with constant in time and space, characterized by a spatially and temporally constant friction coefficient.
 - 2. We propose a new physics-based approach explaining explanation for spontaneous stress drops in deforming rocks, offering potential applications in modeling earthquake triggering for modeling earthquake sequences.
 - 3. We achieve fast computational times using do not prescribe any pre-existing faults; instead, new faults emerge spontaneously from the stress field.
 - 4. We achieve high-resolution models simulations with fast computational performance by leveraging GPU-based parallel computing.

2 Mathematical formulation

80 2.1 Quasi-statics

The conservation of linear momentum is expressed as:

$$\nabla_j \sigma_{ij} + f_i = 0, \tag{1}$$

where σ_{ij} is the stress tensor, f_i is the body force, ∇ is a dell operator, $j = \overline{1..3}$ and Einstein summation convention is applied (summation over repeated indices). The stress tensor is decomposed into bulk (volumetric) and deviatoric components

85
$$\sigma_{ij} = -p\delta_{ij} + \tau_{ij}$$
, (2)

where p is pressure, τ_{ij} is the deviatoric stress tensor, δ_{ij} is the Kronecker delta. The strain rate is defined as

$$\dot{\varepsilon}_{ij} = \frac{1}{2} \left(\nabla_i v_j + \nabla_j v_i \right) \tag{3}$$

The rheology is elasto-plastic, which is characterized by an additive decomposition of the strain rate into an elastic (volumetric and deviatoric) and plastic components

90
$$\dot{\varepsilon}_{ij} = \dot{\varepsilon}_{ij}^{eb} + \dot{\varepsilon}_{ij}^{ed} + \dot{\varepsilon}_{ij}^{pl}, \tag{4}$$

where the superscripts \cdot^{eb} , \cdot^{ed} , \cdot^{pl} denote elastic volumetric (bulk), elastic deviatoric and plastic parts, respectively. The volumetric (bulk) elastic strain rate is

$$\dot{\varepsilon}_{ij}^{eb} = \frac{1}{3} \nabla_k v_k \delta_{ij} = -\frac{1}{K} \frac{\mathrm{D}p}{\mathrm{D}t},\tag{5}$$

the where Dp/Dt is the material derivative (provided in the following section), the deviatoric elastic strain rate is

95
$$\dot{\varepsilon}_{ij}^{ed} = \frac{1}{2G} \frac{\mathcal{D}\tau_{ij}}{\mathcal{D}t},\tag{6}$$

where the Jaumann rate of Cauchy stress deviator of Cauchy stress tensor, represented as $\mathcal{D}\sigma_{ij}/\mathcal{D}t\mathcal{D}\tau_{ij}/\mathcal{D}t$, is provided in the following section and the deviatoric plastic strain rate is

$$\dot{\varepsilon}_{ij}^{pl} = \dot{\lambda} \frac{\partial Q}{\partial \sigma_{ij}},\tag{7}$$

where $\dot{\lambda}$ is the plastic multiplier rate and Q is the plastic flow potential. Combining equations (4)-(7), the total strain rate can be reformulated as

$$\dot{\varepsilon}_{ij} = \frac{1}{2} \left(\nabla_i v_j + \nabla_j v_i \right) = \frac{1}{3} \nabla_k v_k \delta_{ij} - \frac{1}{K} \frac{Dp}{Dt} + \frac{1}{2G} \frac{\mathcal{D}\tau_{ij}}{\mathcal{D}t} + \dot{\lambda} \frac{\partial Q}{\partial \sigma_{ij}}. \tag{8}$$

This the system of equation is the static elasto-plastic model routinely used in solid mechanics (Zienkiewicz and Taylor, 2005).

2.1.1 Large strain formulation

The inelastic response is described using hypoelastic constitutive theory. Hypoelasticity involves formulating the constitutive equations for stress in terms of objective (frame-invariant) stress rates (de Souza Neto et al., 2011). The rate evolution law for stress is as follows (de Souza Neto et al., 2011; De Borst et al., 2012):

$$\frac{\mathcal{D}\sigma_{ij}}{\mathcal{D}t} = \underline{C}^e_{ijkl} \underline{\dot{\varepsilon}}^e_{kl} = \underline{C}^e_{ijkl} (\underline{\dot{\varepsilon}}_{kl} - \underline{\dot{\varepsilon}}^{pl}_{kl}),$$

where C^e_{ijkl} is the elasticity tensor, $\dot{\varepsilon}_{ij} = \dot{\varepsilon}^e_{ij} + \dot{\varepsilon}^{pl}_{ij}$ is the strain rate tensor decomposed into elastic $\dot{\varepsilon}^e_{ij}$ and plastic $\dot{\varepsilon}^p_{ij}$ components.

Since our medium is isotropic, the stiffness tensor C^e_{ijkl} can be fully described by the bulk modulus K and shear modulus G:

The scalar pressure material derivative is represented by the following equation:

$$\underline{C_{ijkl}^{e}} \underbrace{\frac{Dp}{Dt}}_{Dt} = \underline{K - \frac{2}{3}G} \underbrace{\delta_{ij}\delta_{kl}}_{\partial t} \underbrace{\frac{\partial p}{\partial t}}_{t} + \underline{2G} \underbrace{\frac{1}{2}(\delta_{ik}\delta_{jl} + \delta_{il}\delta_{kj})v_{k}}_{\partial t} \underbrace{\frac{\partial p}{\partial x_{k}}}_{t}. \tag{9}$$

The Jaumann rate of Cauchy stress deviator of Cauchy stress tensor, represented as $\mathcal{D}\sigma_{ij}/\mathcal{D}t\mathcal{D}\tau_{ij}/\mathcal{D}t$, is defined by (de Souza Neto et al., 2011):

115
$$\frac{\frac{\mathcal{D}\sigma_{ij}}{\mathcal{D}t}}{\frac{\mathcal{D}\tau_{ij}}{\mathcal{D}t}} = \frac{\frac{\partial\sigma_{ij}}{\partial t}}{\frac{\partial t}{\partial t}} \frac{\partial\tau_{ij}}{\partial t} + v_k \frac{\partial\sigma_{ij}}{\partial x_k} \frac{\partial\tau_{ij}}{\partial x_k} - \dot{w}_{ik}\underline{\sigma}\underline{\tau}_{jk} - \dot{w}_{jk}\underline{\sigma}\underline{\tau}_{ik},$$
 (10)

where \dot{w}_{ij} is the vorticity tensor defined as: $\dot{w}_{ij} = (\nabla_i v_j - \nabla_j v_i)/2$.

2.2 Elasto-dynamics

The conservation of linear momentum is given by extended by addition of inertia:

$$\nabla_j \sigma_{ij} + f_i = \rho \frac{\partial v_i}{\partial t},\tag{11}$$

120 where v is the velocity and ρ is the density. The stress-strain relation is described by:

$$\frac{\partial \sigma_{ij}}{\partial t} = C^e_{ijkl} \left(\underline{\dot{\varepsilon}}_{\underline{k}\underline{l}} - \underline{\dot{\varepsilon}}^{pl}_{\underline{k}\underline{l}} \right),$$

where i, j, k, l = 1, 2, 3.

2.3 Plasticity

130

Plasticity is implemented using a non-associated, pressure-dependent Drucker–Prager criterion (Drucker and Prager, 1952; de Souza Neto et al., 2011; De Borst et al., 2012). According to this criterion, plastic yielding begins when the second invariant of the deviatoric stress, J_2 , and the pressure (minus the mean stress), p, meet the following condition:

$$\sqrt{J_2} - \sin(\varphi)p = \cos(\varphi)c,\tag{12}$$

where c is the cohesion and φ is the angle of internal friction. In terms of the stress tensor, plastic deformations occur when the stresses reach the yield surface. The yield function F and the plastic potential Q for the Drucker-Prager criterion are defined as:

$$F(\tau, p) = \sqrt{J_2 - \sin(\varphi)p - \cos(\varphi)c},\tag{13}$$

where φ is the internal friction angle.

$$Q(\tau, p) = \sqrt{J_2 - \sin(\psi)p},\tag{14}$$

where $\psi \leq \varphi$ is the dilation angle. In two dimensions under plane strain conditions, with $\sigma_{zz} = \frac{1}{2}(\sigma_{xx} + \sigma_{yy})\dot{\epsilon}_{zz} = 0$, the Drucker-Prager criterion is equivalent to the Mohr-Coulomb criterion (Templeton and Rice, 2008). In 2-D, the second invariant of the deviatoric stress, J_2 , is expressed as:

$$J_2 = \frac{1}{2}\tau_{ij}\tau_{ji} = \frac{1}{2}(\tau_{xx}^2 + \tau_{yy}^2 + \tau_{zz}^2) + \tau_{xy}^2.$$
(15)

As long as $F \le 0$, the material remains in the elastic regime. Once F reaches zero (F = 0), plasticity is activated. If the material remains in a plastic state ($\partial F/\partial t = 0$), plastic yielding continues. The current implementation of perfect plasticity requires small time increments and is computationally expensive. To ensure spontaneous strain localization, strain softening is often introduced, which promotes the formation of shear bands (Lavier et al., 1999; Moresi et al., 2007; Popov and Sobolev, 2008; Lemiale et al., 2008). However, there are concerns about the thermodynamic admissibility of such solutions (Duretz et al., 2019). Additionally, the softening or hardening moduli are small compared to the shear modulus and can be neglected as a first-order approximation (Vermeer, 1990), leading to the ideal plasticity model used in the present study.

For the case of regularized plasticity, the the yield function is defined as (Heeres et al., 2002):

$$F(\tau, p) = \sqrt{J_2 - \sin(\varphi)p - \cos(\varphi)c - \eta^{\text{vp}}\dot{\lambda}}.$$
(16)

3 Numerical implementation

3.1 Discretization

140

145

150

155

The numerical domain is discretized using a staggered grid in both space and time (Virieux, 1986). This method provides a variant of the conservative finite volume approach (Dormy and Tarantola, 1995). The total number of grid cells is limited only by the available GPU memory. For the elasto-dynamic equations, an explicit time integration method is employed, offering second-order accuracy in both space and time. Detailed representations of the discrete equations are available in Alkhimenkov et al. (2021). For the quasi-static equations, the discrete scheme achieves second-order accuracy in space. Advection is carried out using an upwind scheme, which is first-order. Consequently, due to the application of the pseudo-transient method, the solution demonstrates first-order accuracy in time (Alkhimenkov and Podladchikov, 2025).

3.2 Accelerated pseudo transient method

The solution of the quasi-static equations is achieved using the matrix-free accelerated pseudo-transient (APT) method (Frankel, 1950; Räss et al., 2022; Alkhimenkov and Podladchikov, 2025). The core concept of this method involves solving dynamic equations with appropriate attenuation of the dynamic fields instead of directly solving inertialess equations. To achieve this, the equations are written in their non-dimensional residual form and iterated over "pseudo-time" until convergence is reached. Once the dynamic fields attenuate to a specific precision (e.g., to 10^{-12}), the solution of the quasi-static equations is attained. In other words, the quasi-static problem serves as an attractor for the dynamic problem with damping. The APT method is

capable of handling numerical domains with more than a billion grid cells. Additionally, since all operations are local, this method can be naturally parallelized using GPUs, which is the approach taken in this study.

165 3.3 Implementation of plasticity

In the return mapping algorithm, the following steps are performed:

1. Calculate the components of the trial deviatoric stresses, τ_{ij}^{trial} . 2. Compute the trial second invariant of the deviatoric stresses, J_2^{trial} , using τ_{ij}^{trial} . 3. Determine F^{trial} using the equation:

$$F^{\text{trial}} = \sqrt{J_2^{\text{trial}} - (\sin(\varphi)p + \cos(\varphi)c)}. \tag{17}$$

When the material is in the plastic state, the trial deviatoric stress components, τ_{ij}^{trial} , are re-scaled according to:

$$\tau_{ij}^{\text{new}} = \tau_{ij}^{\text{trial}} \left(1 - \frac{F^{\text{trial}}}{\sqrt{J_2^{\text{trial}}}} \right) \equiv \tau_{ij}^{\text{trial}} \tilde{\lambda},$$
(18)

where $\tilde{\lambda}=1-\frac{F^{\rm trial}}{\sqrt{J_2^{\rm trial}}}$ is the scaling parameter. This re-scaling process is iterated over "pseudo-time" until the updated trial deviatoric stresses, $\tau_{ij}^{\rm new}$, satisfy the plasticity criterion, ensuring $F^{\rm trial}=0$ (thus, $\tilde{\lambda}=1$ and no re-scaling occurs). A regularized version of this procedure modifies formula (18) to (assuming non-zero dilatation angle ψ):

175
$$\tilde{\lambda} = 1 - \frac{F^{\text{trial}} \Delta t G^{\text{e}}}{\sqrt{J_2} (G^{\text{e}} \Delta t + K \Delta t \sin \varphi \sin \psi + \eta^{\text{vp}})}$$
 (19)

where $\eta^{\rm vp}$ is the viscosity of the damper (regularization parameter) regularization parameter having units of viscosity. [$Pa \cdot s$]. The numerical viscosity $\eta^{\rm vp}$ is usually set to a small value. If this value is too high, the shear bands become very thick; conversely, if the value is too small, the thickness of the shear band is just one pixel. The correct value of the viscosity damper lies between these limits. In the following section, we examine how the choice of viscosity damper affects the solution. This implementation of plasticity through re-scaling deviatoric stress components is equivalent to the standard procedure using the plastic multiplier rate, $\dot{\lambda}$, which is defined as

$$\dot{\lambda} = \frac{F^{\text{trial}}}{\Delta t G^{\text{e}} + K \Delta t \sin \varphi \sin \psi + \eta^{\text{vp}}}.$$
(20)

For a more detailed explanation of how plasticity with regularization is implemented in single-phase media, refer to Duretz et al. (2018, 2019, 2021).

185 3.4 Nondimensionalization

180

3.4 Model configuration, boundary conditions, and non-dimensionalization

The computational domain is a square with dimensions $x,y \in [0,L_x] \times [0,L_y] x, y \in [-L_x/2,L_x/2] \times [-L_y/2,L_y/2]$. All simulations in this study are performed using a simple initial model configuration and non-dimensional equations. To ensure a consistent dimensionless framework, we define the following characteristic scales: length $l^* = L_x$, and time $t^* = 1/a$, and

pressure $p^* = G_0$. Here, L_x represents the domain size in the x-direction, $L_x = L_y = 1$ and a denotes the background strain rate. Deformation evolves over timescales inversely proportional to the initial background strain rate a_0 at t = 0. The ratio of cohesion c to the pressure scale p^* is defined as $r = \frac{c_0}{G_{0x}}$, $G_0 = 1$ and $c_0 = 10^{-2}$.

For all computations, we set the coefficient of internal friction to $\mu = 0.6 \mu = 0.5$. Pure shear boundary conditions are applied by prescribing velocities at all boundaries in the dimensionless frameworknormal velocities at the left and right boundaries:

$$195 \quad v_x = ax \tag{21}$$

and at top and bottom boundaries

$$v_y = -ay, (22)$$

which corresponds to the extension in x-dimension and compression in y-dimension. We impose loading increments applied to the strain components. At all boundaries, free-slip boundary conditions are implemented. The following initial conditions are implemented: p = 0,

$$p\tau_{xx} = 0.004c_0, \tag{23}$$

$$\tau_{\underline{xxyy}} = \underline{0.012, -c_0}.\tag{24}$$

205 $\tau_{yy} = -0.012$.

200

We introduce a circular inclusion in the non-dimensional pressure pcohesion c, representing a localized increase with the highest value at the center of the modelstiff inclusion. The expression in the dimensionless framework is as follows:

$$\underline{pc} = \begin{cases} 2c_0, & \text{if } \sqrt{(x + L_x/10)^2 + (y + L_y/5)^2} < 0.0625^2, \\ c_0, & \text{otherwise.} \end{cases}$$
 (25)

We impose loading increments applied to the strain components.

210 4 Results

4.1 Low resolution simulation Integrated stress σ_{xx}^{INT}

In our low-resolution simulations (Figure ??), we observe that To analyze the evolution of the integrated stress simulated system, we evaluate the integrated axial stress σ_{xx}^{INT} follows a monotonic trend, with no discernible stress drops. This outcome aligns with the coarse spatial discretization of $N=63^2$ grid cells, wherein finer stress and strain variations cannot be accurately captured. The integrated stress σ_{xx}^{INT} is computed over along a vertical line segment using the following expression:

$$\sigma_{xx}^{\text{INT}} = \frac{1}{L_y} \int_0^{L_y} \left(\left(-p(x_0, y) + \tau_{xx}(x_0, y) \right) \right) dy, \tag{26}$$

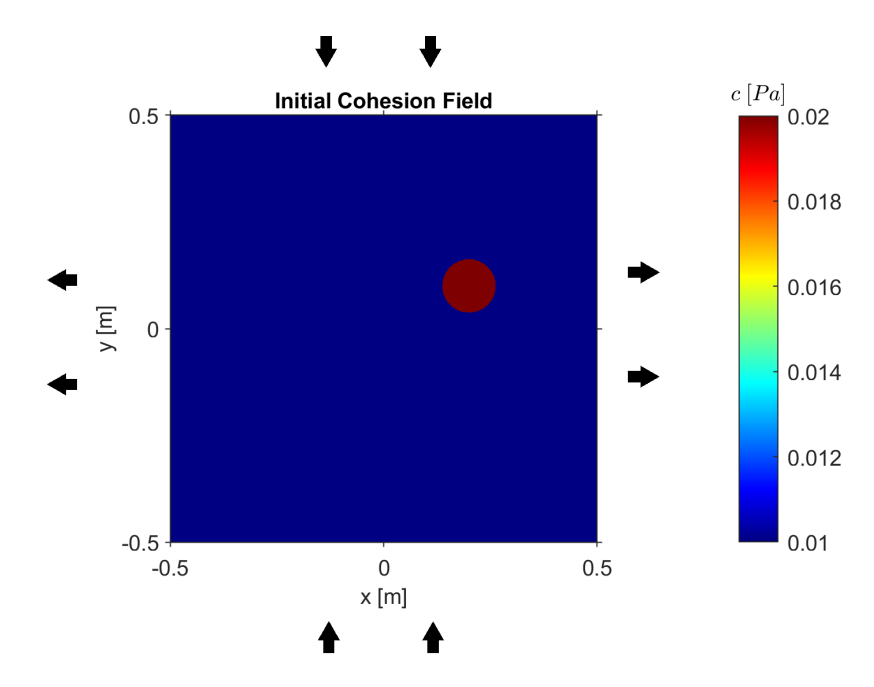


Figure 1. Heterogeneous initial setup of pressure pcohesion c. The arrows indicate the pure shear boundary condition which is applied at the model boundaries.

where x_0 is a fixed coordinate in x-dimension. The strain localization patterns observed in the pressure and strain rate fields remain symmetric throughout the loading process, indicating a relatively uniform distribution of deformation. This result is expected in low-resolution simulations, where the model's ability to resolve localized strain structures, such as shear bands or deformation zones, is limited by the grid resolution, the x-direction $(x_0 = L_x/4)$.

Moreover, in low-resolution models, the regularization parameter $\eta^{vp} = 6 \times 10^{-4}$ plays a critical role in smoothing out any potential irregularities in the stress field. While this helps stabilize the model numerically, it also suppresses any potential stress drops. The absence of stress drops in low-resolution simulations suggests that grid refinement is necessary to capture more detailed stress and strain distributions, which could better reflect the underlying physical processes driving seismicity

4.1.1 Convergence study

220

225

230

To determine the necessary spatial and temporal resolutions (i.e., the resolution with respect to loading increments), we performed a convergence study. Simulations were conducted with different spatial resolutions, ranging from $N = 63^2$ to $N = 2047^2$, while keeping the regularization viscosity constant across all cases. The results are shown in Figure 2.

Low resolution simulation. Panel (a) shows the integrated stress σ_{xx}^{INT} versus strain increments, panels (b-d) show pressure p for at three different stages of the simulation, panels (e-g) show $\log_{10}\epsilon_{II}$ and panels (h-j) show $\log_{10}\dot{\epsilon}_{II}$.

4.2 Sufficient resolution simulation

235

240

245

250

255

260

In contrast, our sufficient resolution simulations with $N=1023^2$ grid cells reveal several significant stress drops (Figure ??), suggesting that the model resolution is now capable of accurately capturing the dynamic changes in stress during loading. The regularization parameter is set to $\eta^{\rm vp}=1\times 10^{-5}$. The stress dropscorrespond to instances of rapid strain localization, where non-symmetric shear bands develop and propagate throughout the model domain. These shear bands form due to the onset of plastic yielding, which is triggered as local stresses surpass the material's yield strength. This non-symmetric strain localization is a hallmark of plastic deformation and closely resembles the behavior observed in laboratory experiments on rock deformation, where similar patterns of localized shear zones have been reported (Johnson et al., 2008; Scuderi et al., 2016).

Furthermore, the higher resolution provides clearer insights into the spatial structure of the stress and strain fields, revealing the complex, non-uniform distribution of deformation during stress drop. Notably, the stress drops become more pronouncedand sharper as the temporal resolution is increased, underscoring the importance of both spatial and temporal refinement in accurately capturing the dynamics of At low resolution (e.g., $N=63^2$), the model does not capture sharp stress drops. However, as resolution increases, stress accumulation and releasedrops become increasingly pronounced. Notably, both the amplitude and clarity of the stress drops converge for resolutions of $N=1023^2$ and higher.

4.1.1 Mohr's circle analysis

Figure?? illustrates the stress state of the material through a Mohr's circle representation at two critical stages: the beginning of loading (panel (a)) and after shear band localization (panel (b)). Mohr's circle is a graphical tool used to represent the state of stress at a point, plotting the normal and shear stresses acting on different planes through that point.

In panel (a) , the stress is evenly distributed, and Figure 3 illustrates the strain localization pattern at time t_3 for four different resolutions. Starting at $N=1023^2$, the circle lies within the elastic regime. The material is in equilibrium, with no plastic yielding or localized strain. This initial Mohr's circle is small, reflecting the lower stress magnitudes early in the loading process. The friction coefficient is $\mu_{\text{true}}=0.6$, which corresponds to $\varphi_{\text{true}}\approx 31^\circ$. Note that $\tan(\varphi_{\text{true}})=\tan(31^\circ)\approx 0.6$ structure and distribution of shear bands remain qualitatively similar, indicating convergence of the deformation pattern.

Panel (b) shows Mohr's circle after the onset of strain localization, coinciding with a significant stress drop in the simulation. As loading progresses and the material begins to yield, Mohr's circle shifts, reflecting the decrease in pressure as the system approaches the yield criterion. The expansion of Mohr's circle towards the yield envelope indicates that the material has reached its plastic limit, and shear bands begin to localize. We also highlight additional intersections along the yield envelope.

Of particular importance is the angle $\varphi_{apparent} \approx 27^{\circ}$ (estimated numerically by analyzing the green triangle, Figure $\ref{eq:particular}$), which is the apparent angle related to the apparent coefficient of friction $\mu_{apparent}$. According to Byerlee and Savage (1992), the value of μ_a is always lower than the real coefficient of internal friction, μ . There is a theoretical formula that relates $\mu_{apparent}$ The total (Eulerian) displacement in the χ - and μ_{true} (see Figure $\ref{eq:particular}$):

$$\mu_{\mathrm{apparent}} = \sin(\arctan \mu_{\mathrm{true}}) \equiv \sin(\arctan 0.6) \approx 0.51$$

y-directions is updated from the velocities using

$$u_x^{(n)} = u_x^{(n-1)} + v_x^{(n)} \Delta t, \qquad u_y^{(n)} = u_y^{(n-1)} + v_y^{(n)} \Delta t. \tag{27}$$

The theoretical value of $\mu_{apparent} = 0.51$ provides us with $\varphi_{apparent} = \arctan(0.51) \approx 27^{\circ}$, which is the same value estimated numerically by analyzing the green triangle (see paragraph above and Figure ?? where n and n-1 denote the current and previous time steps, respectively. The incremental (Eulerian) displacement is then given by

$$\Delta u_x = u_x^{(n)} - u_x^{(n-1)}, \qquad \Delta u_y = u_y^{(n)} - u_y^{(n-1)}. \tag{28}$$

Strain components are computed from (Eulerian) displacement gradients as

$$\underbrace{\nabla \cdot \mathbf{u}}_{=} \frac{\partial u_x}{\partial x} + \frac{\partial u_y}{\partial y}, \tag{29}$$

$$\varepsilon_{xx} = \frac{\partial u_x}{\partial x} - \frac{1}{3}\nabla \cdot \mathbf{u},\tag{30}$$

$$\underbrace{\varepsilon_{yy}}_{yy} = \frac{\partial u_y}{\partial y} - \frac{1}{3} \nabla \cdot \mathbf{u},\tag{31}$$

$$\varepsilon_{xy} = \frac{1}{2} \left(\frac{\partial u_x}{\partial y} + \frac{\partial u_y}{\partial x} \right). \tag{32}$$

Finally, the (Eulerian) deviatoric strain measure is defined as

280

285

275
$$J_2^u = \sqrt{\frac{1}{2} \left(\varepsilon_{xx}^2 + \varepsilon_{yy}^2\right) + \varepsilon_{xy}^2}.$$
 (33)

A zoomed-in view of $\log_{10}(J_2^u)$ field is provided in Figure 4, where we observe that the thickness of the shear bands spans several grid cells even at $N=511^2$ (panel a), and more than ten grid cells at $N=1023^2$ (panel b). The reduced apparent coefficient of friction is a consequence of plastic flow in the plastic zone, which allows slip to occur more easily along the shear band, despite the actual slip occurring along the Coulomb shear planes. This confirms that the regularization is effective—if it were not, the shear bands would collapse to 1-3 grid cells irrespective of resolution.

Figure 5 shows the pressure field p at time t_3 for four spatial resolutions. As resolution increases from $N=511^2$ to $N=2047^2$, finer pressure structures become apparent, highlighting the emergence of sharp gradients. All snapshots correspond to a total strain of $\varepsilon=0.04$. Based on these results, we conclude that a resolution of $N=1023^2$ is sufficient for capturing both stress drop dynamics and shear band structure while maintaining a balance between accuracy, computational cost, and memory requirements.

4.2 Focusing on stress drops, quasi-static interseismic period and dynamic modeling of the transition between quasi-static interseismic periods

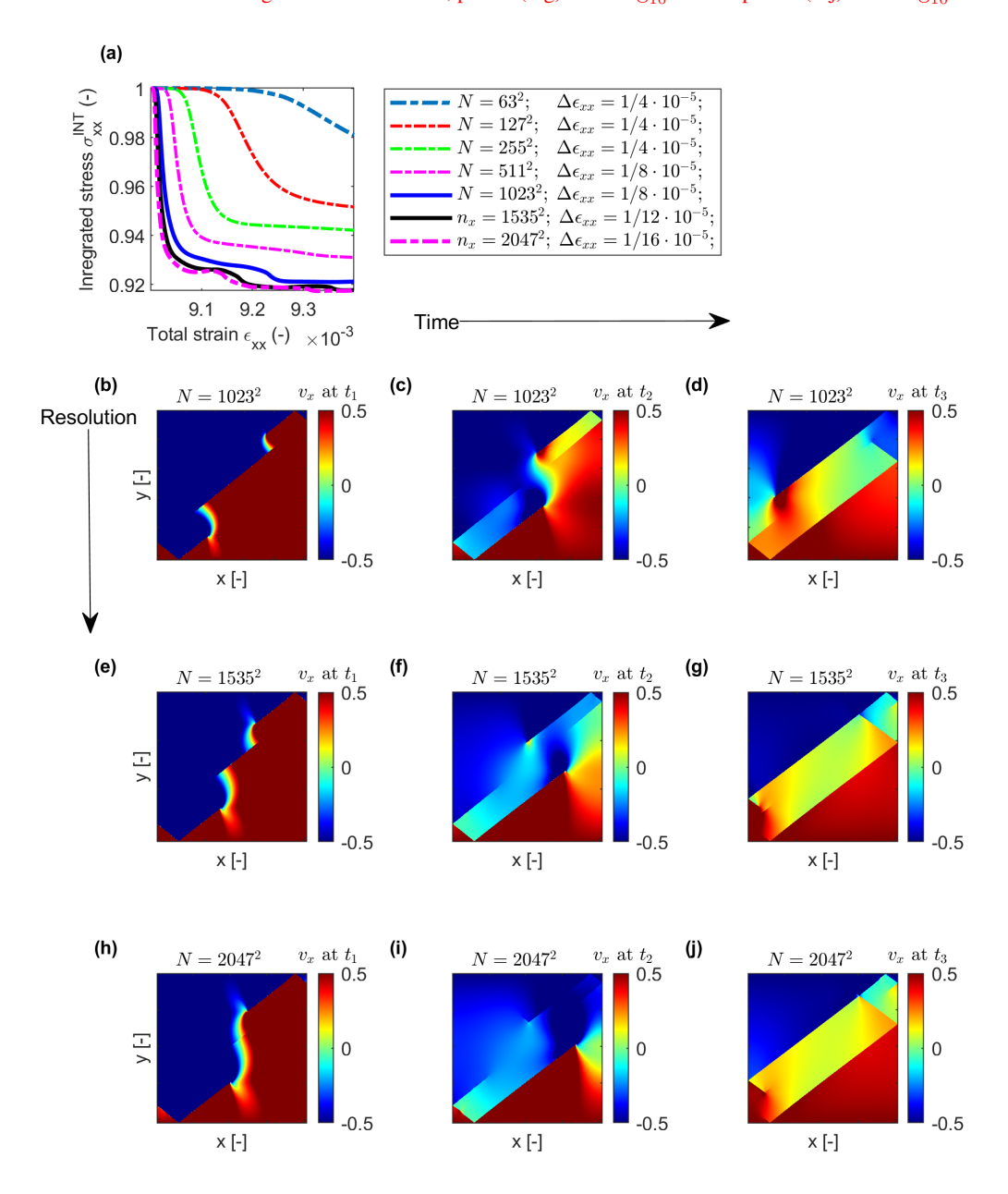


Figure 2. Convergence study. Panel (a) shows the integrated stress $\sigma_{xx}^{\rm INT}$ as a function of total strain for multiple resolutions. Panels (b-j) show the velocity field v_x at three different time steps (t_1-t_3) and three different resolutions: $N=1023^2$, $N=1535^2$, $N=2047^2$. t_1 corresponds to the total strain $\varepsilon=0.022$, t_2 corresponds to the total strain $\varepsilon=0.026$, and t_3 corresponds to the total strain $\varepsilon=0.04$. Regularization parameter is $\eta^{\rm vp}=1/2:10^{-5}$ in all simulations.

Mohr's circle diagram. Stress state before and after strain localization. This diagram shows that the true friction angle φ_{true} is always greater than or equal to the apparent friction angle $\varphi_{\text{apparent}}$. The relation between the true and apparent friction coefficients is

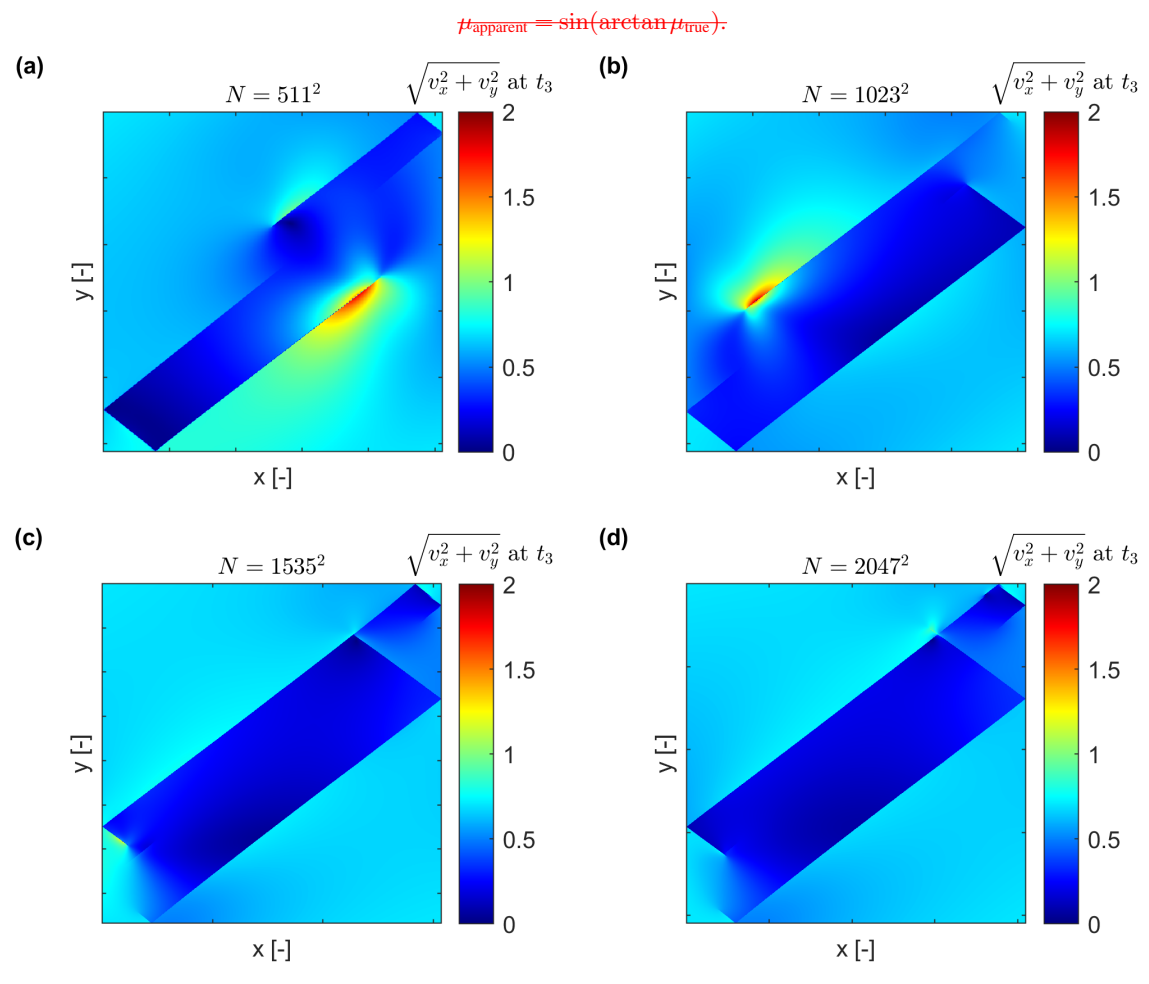


Figure 3. The total velocity field $\sqrt{v_x^2 + v_y^2}$. Simulations at t_3 for four different resolutions: $N = 511^2$, $N = 1023^2$, $N = 1535^2$, and $N = 2047^2$. t_3 corresponds to the total strain $\varepsilon = 0.04$.

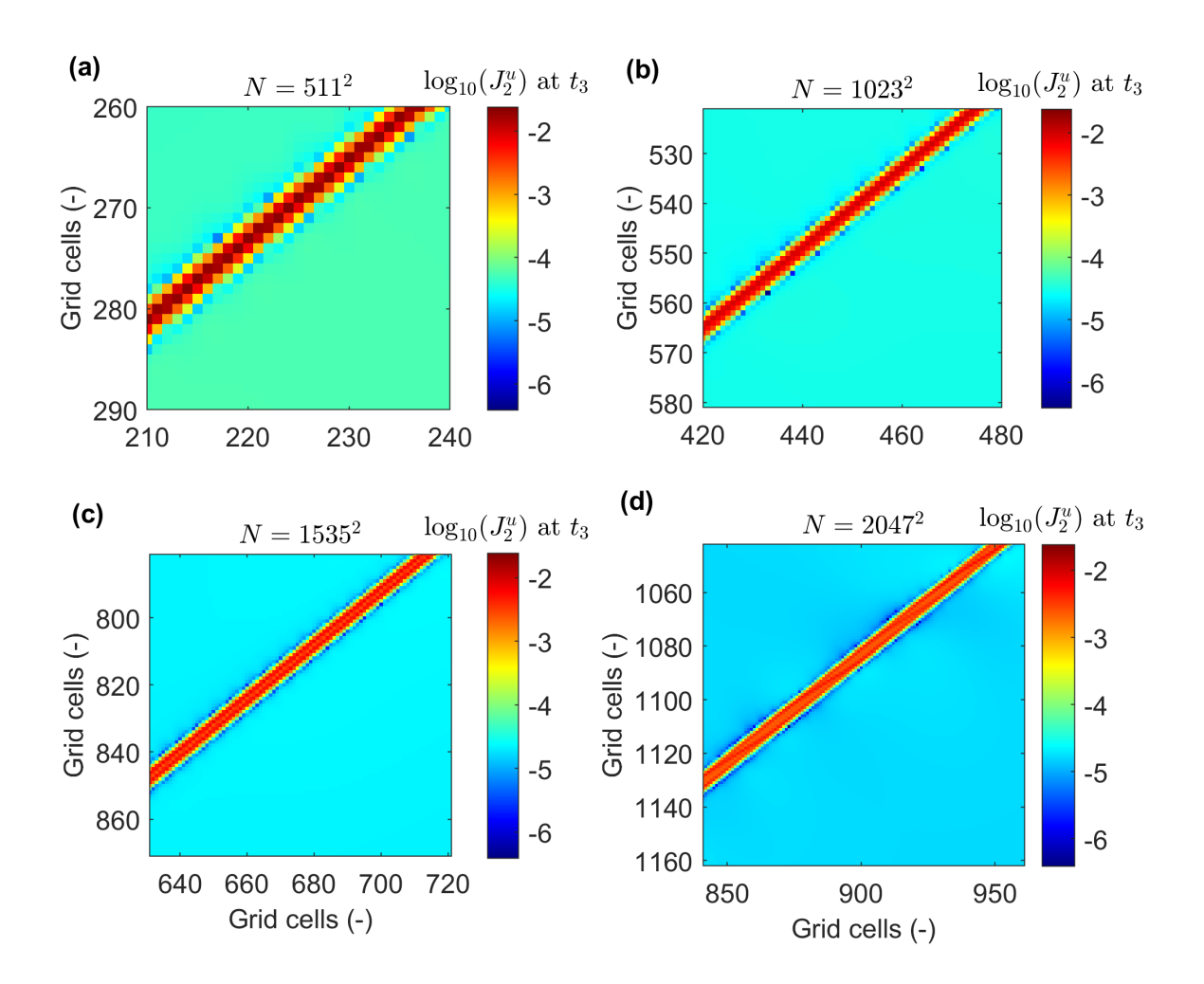


Figure 4. $\log_{10} J_2^u$ field. Zoomed-in view of simulations at t_3 for four different resolutions: $N = 511^2$ (panel a), $N = 1023^2$ (panel b), $N = 1535^2$ (panel c), and $N = 2047^2$ (panel d). t_3 corresponds to the total strain $\varepsilon = 0.04$.

Figure?? shows the numerical simulation with focus on stress drops and interseismic periods. For example, u_x corresponding to stress drop 1 is calculated as $u_x = u_x(t_2) - u_x(t_1)$, where t_1 corresponds to the total strain just before the stress drop (first red circle) and t_1 corresponds to the total strain just after the stress drop (second red circle). The calculation of u_x corresponding to the interseismic period 1 is similar: $u_x = u_x(t_3) - u_x(t_2)$, where t_2 corresponds to the total strain just after the stress drop 1 (second red circle) and t_3 corresponds to the total strain just before the stress drop 2 (third red circle).

290

295

Stress drop manifest the jump between the two quasi-static solutions and perhaps indicate the absence of a static transition between the stress state at the end interseismic period and onset of a new interseismic period.

This transition can be modeled with simplified linear elasto-dynamics by setting the difference in strain just before and after a stress drop as an initial condition for wave propagation.

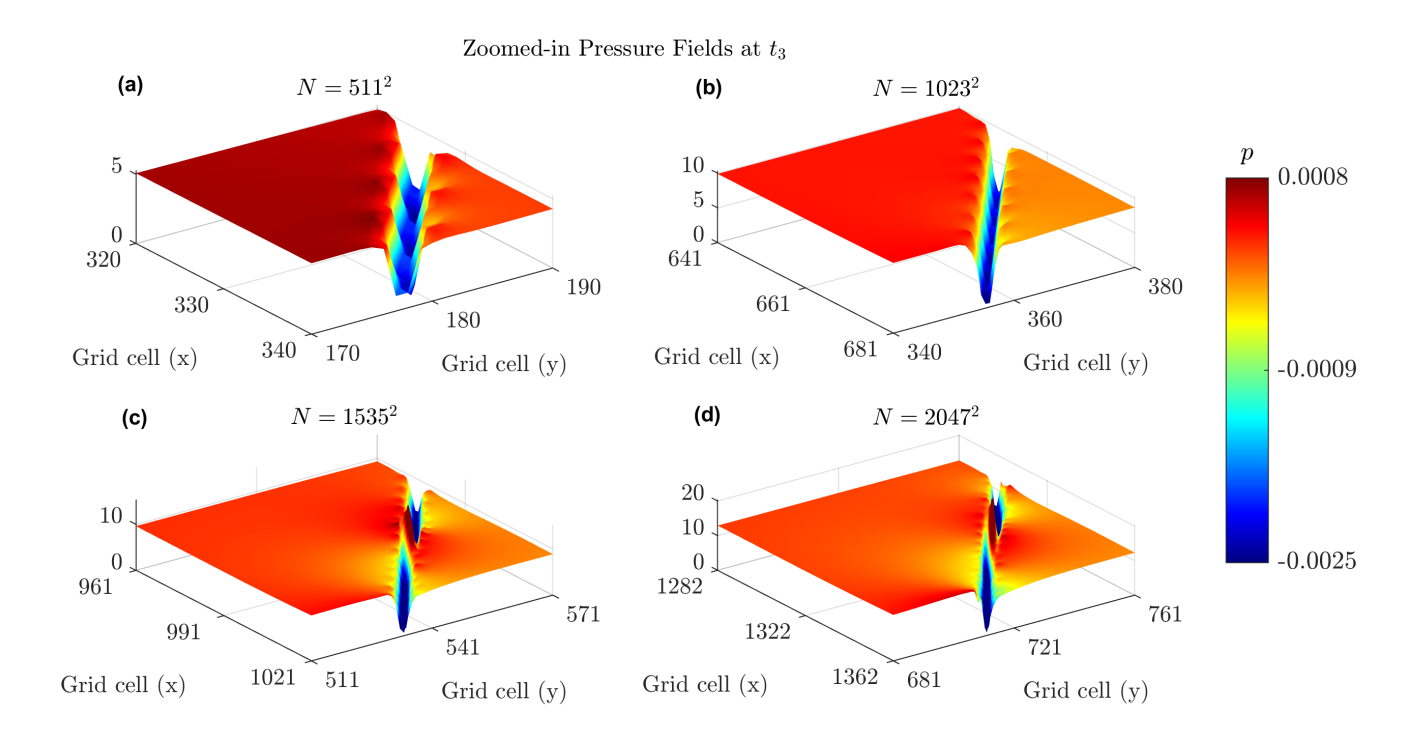


Figure 5. Stress drops and interseismic periods: numerical simulation of compressible elasto-plastic equations with the resolution of $N=1023^2$ grid cellsPressure field p. Panel Zoomed-in view of simulations at t_3 for four different resolutions: $N=511^2$ (panel a)shows the integrated stress σ_{xx} versus strain increments. Panels, $N=1023^2$ (panel b,d,f,h)show displacement increments Δu_x corresponding to stress drops and interseismic periods. Panels, $N=1535^2$ (panel c), e,g,iand $N=2047^2$ (panel d)show pressure increments Δu_x corresponding. t_3 corresponds to stress drops and interseismic periods the total strain $\varepsilon=0.04$.

4.2 Trends

5 Earthquake sequence

5.0.1 Trends with increasing temporal resolution

First, we conduct a temporal convergence test (Figure ??). Using a spatial resolution of $N=511^2$ grid cells, simulations are performed with strain increments $\Delta\epsilon_{xx}=1\times10^{-5}$ In this section, we analyze the stress response of the system over a complete loading cycle comprising $16, \Delta\epsilon_{xx}=4\times10^{-5}000$ incremental steps. We focus on three aspects: (i) the sequence of stress drops that emerge as strain accumulates, (ii) the statistical distribution of these drops, $\Delta\epsilon_{xx}=10\times10^{-5}$. It is observed that the evolution of the integrated stress $\sigma_{xx}^{\rm INT}$ with strain increments is converging to a specific pattern as the number of increment increasing. Simulations with finer temporal discretization result in slightly sharper drops in $\sigma_{xx}^{\rm INT}$, and (iii) the wavefield dynamics resulting from a single stress drop event. All results presented in this section are obtained from a fully converged simulation with spatial resolution $N=1023^2$, constant regularization viscosity, and pseudo-transient iterations that ensure convergence at each step.

Trends with increasing temporal resolution. Panel (a) shows the integrated stress σ_{xx}^{INT} versus strain increments. Panels (b,e,d,e) show displacement increments Δu_x corresponding to stress drops and interseismic periods that correspond to $\Delta \epsilon_{xx} = 1 \times 10^{-5}$. Panels (f,g,h,i) show pressure increments Δu_x corresponding to stress drops and interseismic periods that correspond to $\Delta \epsilon_{xx} = 4 \times 10^{-5}$. Panels (j,k,l,m) show pressure increments Δu_x corresponding to stress drops and interseismic periods that correspond to $\Delta \epsilon_{xx} = 10 \times 10^{-5}$.

5.1 Numerical convergence and stability

315 5.1.1 Trends with increasing spatial resolution

320

To investigate the dependence of the integrated stress $\sigma_{xx}^{\rm INT}$ versus spatial resolution, we conduct experiments with spatial discretizations of $N=63^2$ To ensure that the stress drops analyzed in this study arise from physically meaningful simulation, $N=1023^2$, and $N=2047^2$ (Figure 2). Note that we re-scale the viscosity damper proportionally to the resolution in each simulation to maintain the physical thickness of the shear bands Alkhimenkov et al. (2024b). It can be seen that the low resolution simulation $N=63^2$ does not produce any stress drops. However, simulations with sufficient resolution produce stress drops and their amplitudes are similar.

Trends with increasing spatial resolution. Panel (a) shows the integrated stress $\sigma_{xx}^{\rm INT}$ versus strain increments. Panels (b,c,d,e) show displacement increments Δu_x corresponding to stress drops and interseismic periods that correspond to $N=63^2$ grid cells. Panels (f,g,h,i) show pressure increments Δu_x corresponding to stress drops and interseismic periods that correspond to $N=1023^2$ grid cells. Panels (j,k,l,m) show pressure increments Δu_x corresponding to stress drops and interseismic periods that correspond to $N=2047^2$ grid cells.

5.1.1 Effect of the regularization

330

335

345

350

355

Figure ?? shows the simulation results for different spatial discretizations of $N=63^2$, $N=255^2$, and $N=1023^2$ grid cells. Due to high regularization, the results are nearly identical and the thickness of the shear bands is the same in all panels. However, due to over-regularization, the stress drop is not visible.

Effect of the regularization. Panel (a) shows the integrated stress $\sigma_{xx}^{\rm INT}$ versus strain increments. Panels (b,c,d,e) show displacement increments Δu_x corresponding to stress drops and interseismic periods that correspond to $\eta^{\rm vp}=0$. Panels (f,g,h,i) show pressure increments Δu_x corresponding to stress drops and interseismic periods that correspond to $\eta^{\rm vp}=1\times 10^{-5}$. Panels (j,k,l,m) show pressure increments Δu_x corresponding to stress drops and interseismic periods that correspond to $\eta^{\rm vp}=10\times 10^{-5}$. The resolution is $N=511^2$ grid cells in all simulations).

Effect of the regularization. Panel (a) shows the integrated stress σ_{xx}^{INT} versus time, panels (b-d) show $\log_{10} \epsilon_{II}$ for a set of different spatial discretizations: $N = 63^2$, $N = 255^2$, and $N = 1023^2$ grid cells.

5.2 High-resolution simulation

The high-resolution simulationis performed with a grid size of $N=4095^2$, allowing for the capture of finer details in the stress, strain, and pressure fields. In these simulations, the component $\log_{10} \epsilon_{II}$ is used to represent the second invariant of the deviatoric strain rate tensor, which highlights zones of intense strain localization, typically corresponding to regions where shear bands form.

As shown in Figure??, the regularization applied is sufficient to resolve pressure drops and observe localized strain structures across multiple grid cells. The use of such a fine grid provides enhanced spatial resolution, allowing us to capture more realistic patterns of strain localization that resemble those seen in natural seismic zones, where shear bands and strain concentrations often precede fault rupture or failure events.

Additionally, Figure ?? presents a zoomed-in view of these strain localization features as a 3D plot. In this plot, the vertical axis (z-dimension) corresponds to the amplitude of the pressure field p (Figure ??a) and we monitor the convergence behavior of the $\log_{10} \epsilon_{IT}$ (Figure ??b pseudo-transient iterations used to solve the elasto-plastic equations at each time step. Figure 6 shows the number of iterations required per physical time step (top panel), the corresponding final residual at convergence (middle panel), and the residual curve versus pseudo-time iterations for the final step (bottom panel). The localized shear band thickness is clearly visible, indicating zones of intense deformation and stress concentration. Such fine-scale detail is critical for accurately modeling the mechanics of earthquake triggering, where small variations in stress and strain fields can have significant impacts on rupture initiation and propagation residual error is calculated using the L^{∞} norm. The number of iterations per step remains moderate throughout the simulation, and the final residuals consistently remain below a prescribed

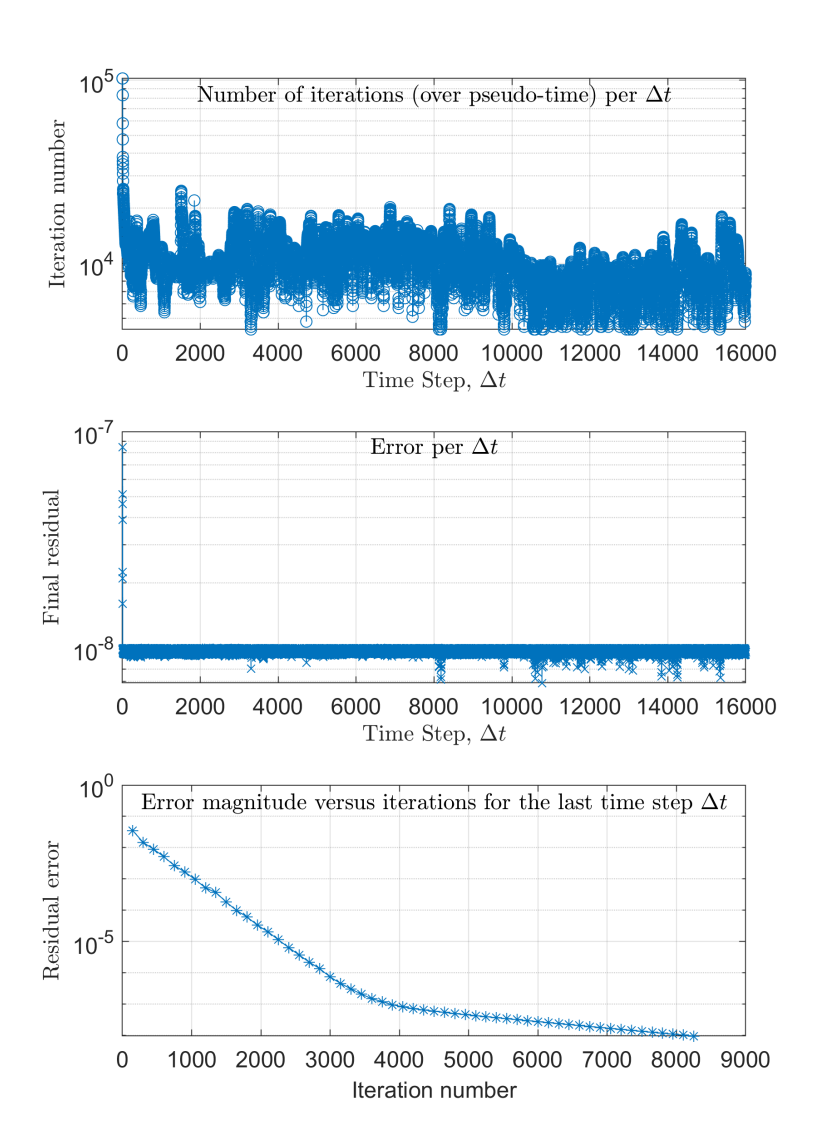


Figure 6. Panel (a) shows $\log_{10} \epsilon_{IT}$ Convergence diagnostics for pseudo-transient iterations. Panels (b) corresponds to zoom-in focusing on a single shear band thickness Top: Number of iterations per physical time step. Middle: Final residual error per time step. Bottom: Residual magnitude versus iteration number for the final time step.

threshold, confirming that the nonlinear solver converges consistently even during dynamic events such as stress drops. These diagnostics support the reliability of the stress evolution and wavefield results presented in the following subsections.

Zoom-in result for the spatial discretizations of $N=4095^2$ as a 3D plot where z-dimension corresponds to the amplitude of the pressure field, p.

5.2 Final velocity and pressure fields

365 5.3 Dilataney

370

380

385

390

Dilatancy refers to the volumetric expansion that occurs in a material when it undergoes shear deformation, particularly under conditions of plastic flow. This phenomenon is especially important in the study of earthquake mechanics, as it affects the porosity and fluid flow within fault zones, and hence, influences the strength and failure behavior of the fault.

In Figure $\ref{eq:property}$, numerical simulations are performed for different values of the dilatation angle ψ , representing different degrees of dilatancy in the material. The results illustrate the effect of the dilatation angle on strain localization and fault weakening. For a small dilatation angle ($\psi=5^{\circ}$), the material exhibits relatively limited volumetric expansion during shear deformation, leading to more localized strain and narrower shear bands. This corresponds to less energy dissipation and a more brittle-like failure response.

As the dilatation angle increases to a moderate value ($\psi = 15^{\circ}$), the material shows more volumetric expansion, which slightly widens the shear bands and leads to a more diffuse strain localization pattern. This represents a more duetile response, where plastic deformation is distributed over a broader zone.

In the case of $\psi=30^\circ$, corresponding to the associated plasticity model, the volumetric expansion is maximized, and the shearbands become much broader. This behavior reflects greater energy dissipation, as the material undergoes significant volumetric changes during shear deformation. The associated plasticity model is typically used for materials that exhibit a strong dilatant response, such as certain types of granular soils or fractured rocks.

For comparison, Figure ?? shows numerical results for $\psi=0^\circ$ The final velocity and pressure distributions highlight the complex flow and $\varphi=0^\circ$, which correspond to the plasticity behavior typically observed in metals. In this case, the material does not exhibit any volumetric expansion during shear deformation, leading to purely deviatoric plastic flow. The absence of dilatancy results in narrow and highly stress responses at the end of the simulation, as shown in Figure 7. The velocity field v_x exhibits sharp gradients in zones of intense shear, while the solid-phase pressure p shows localized shear bands, as expected in materials that do not undergo volumetric changes. This behavior is characteristic of metals under plastic deformation, where energy dissipation is minimized, and the material response remains predominantly brittle. These results underscore the contrasting effects of dilatancy on shear band formation and highlight the unique deformation mechanisms in metallic versus dilatant materials.

Numerical results for $\psi = 0$ and $\varphi = 0$, corresponding to the plasticity behavior of metals.

5.3 Stress drops

5.4 Stress drop sequence

Figure 8 presents the integrated evolution of integrated axial stress σ_{xx}^{INT} versus time (Figure 8a) for different temporal resolutions. Figure 8b shows the zoomed in plot where sharp stress drops can be visible. The stress drops exhibit varying

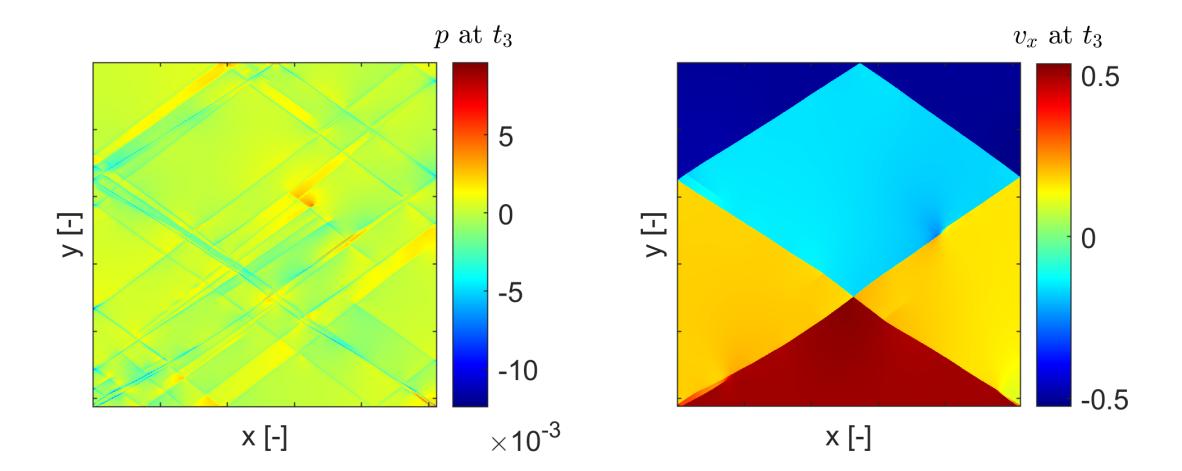


Figure 7. Numerical results for different angles ψ , where $\psi = 5^{\circ}$ corresponds to the small dilatation angle, $\psi = 15^{\circ}$ corresponds to the moderate dilatation angle, Final spatial fields of velocity v_x and $\psi = 30^{\circ}$ corresponds to the associated plasticity solid pressure p after 16000 incremental steps.

395 magnitudes and irregular spacing. The simulation with fine temporal resolution and the lowest regularization corresponds to the sharpest stress drops (blue curve). The simulations with low temporal resolution does not present a proper stress drops.

During as a function of total applied strain for 16,000 loading increments. The main panel (Figure 8a) shows the full sequence, while the three lower panels provide zoomed-in views of the early (0–1/3), middle (1/3–2/3), and late (2/3–1) loading stages, where individual stress drops become clearly visible. Throughout the loading process, numerous stress drops are observed (Figure 8). These stress. These drops correspond to sudden shifts abrupt changes in the system²'s stress state, where the occurring when strain localization reaches a critical point, threshold and further deformation in the prescribed direction becomes untenable. As a resultunsustainable. At these points, the system undergoes a rapid redistribution of stress stress redistribution, manifested as a drop discrete decreases in the integrated stress σ_{xx}^{INT} .

400

405

These stress drops events are indicative of dynamic rupture events, akin to rupture-like behavior, resembling the rapid stress release observed that occurs during seismic slip in natural earthquakes. However, we admit note that in this first initial study, we only indicate this similarity focus only on the qualitative resemblance and do not provide a detailed analysis of slip rate and rupture speeds in the present model. The rates or rupture propagation speeds. The observed sequence of stress drops observed in the simulation resembles the cyclic mimics the typical behavior of fault systems, where interseismic periods of stress accumulation are interrupted by seismic events. By increasing the temporal resolution, we capture sharper, more distinct

stress drops, highlighting the need for high-resolution models to accurately represent seismic processes. sudden stress release events. This behavior supports the interpretation of the model as capturing essential features of earthquake cycles within an elasto-plastic framework.

5.3.1 Histogram of stress drop amplitudes

425

430

435

440

The histogram of stress drop amplitudes shown in Figure 9 provides a quantitative representation of the frequency and magnitude of stress drops occurring during the simulations observed over the course of the full simulation (16,000 loading increments). The distribution of stress drop amplitudes is notably is clearly non-Gaussian, characterized by a broad peak with long tails on both sides, indicating that while small spanning more than five orders of magnitude in amplitude. It is unimodal and asymmetric, with a pronounced peak near $\log_{10}(\Delta\sigma) \approx -4.5$ and long tails toward both smaller and larger events. Small stress drops are more common, larger stress drops still occur with significant probability. This distribution resembles significantly more frequent, but large-magnitude stress releases are still present.

This behavior is reminiscent of turbulence-like spectrum, where a few large events (bursts) coexist with numerous smaller fluctuations. For solid systems, this phenomenon was first analyzed by Poliakov et al. (1994), who explored the multi-fractal characteristics of shear bands spectra in other complex systems, where intermittent bursts coexist with background fluctuations. In the context of solid deformation, this has been described as "solid turbulence" and was first explored by Poliakov et al. (1994), who analyzed the multifractal structure of shear localization in elasto-plastic media, that makes it similar to the fluid turbulence.

Figure 9b presents three histograms of stress drop amplitudes corresponding to very small strain increments, providing high-resolution data. The overall pattern across the histograms is similar, indicating the convergence of our results. In Figure 9e, two histograms are shown: one for a high-resolution loading increment ($\Delta\epsilon_{xx}=1\times10^{-5}$) and the other for the lowest resolution used in this study ($\Delta\epsilon_{xx}=100\times10^{-5}$). The difference between these two is substantial, demonstrating that the low-resolution case fails to capture the full spectrum of stress drop amplitudes. Lastly, Figure 9d compares four histograms at high, intermediate, and low resolutions for further comparison.

In the context of our elasto-plastic. In our model, the non-Gaussian-broad-tailed nature of the histogram suggests reflects a complex interaction between localized plastic yielding and the broader elastic response of the material. Just as yield and global elastic stress redistribution. As in fluid turbulence,—where energy cascades from large to small scales, in solid turbulence, stress—stress in the solid is redistributed across different multiple spatial and temporal scales, leading to a range of stress drop magnitudes. This complex behavior highlights the inherent intermittency and unpredictability in the system's response, where stress accumulates gradually but is released in sudden, sporadic bursts during stress drops, intermittent bursts of plastic deformation.

Understanding the solid turbulence-like behavior in these systems this type of emergent behavior is crucial for developing accurate models of modeling seismicity, where stress drops correspond to represent analogs of earthquake events. The implications of this behavior are significant for earthquake hazard assessment, as it suggests that a wide range of earthquake magnitudes should be expected, with smaller events being far more frequent than larger ones. This insight suggests a resemblance to the

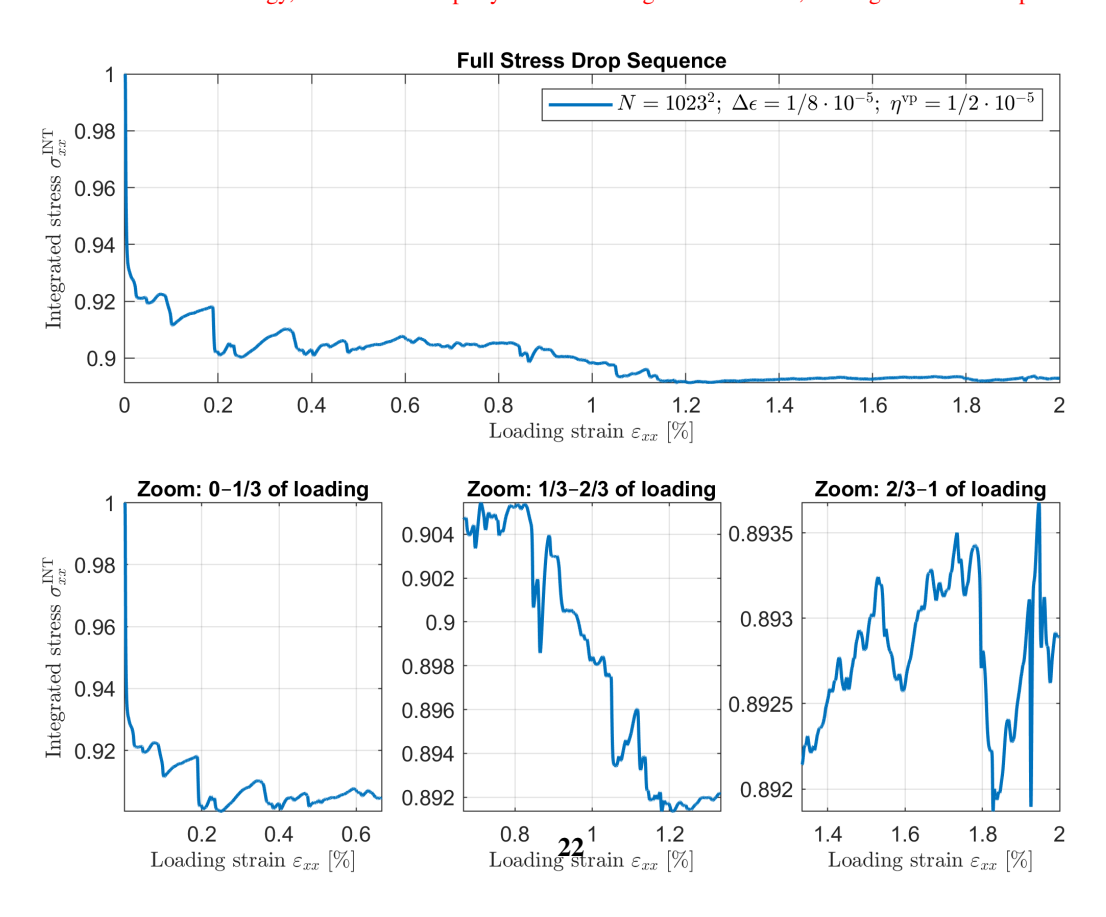
Numerical simulation of elasto-plastic equations with the resolution of 1023^2 grid cells for 2500 loading increments in time. Panel (a) shows the integrated stress $\sigma_{xx}^{\rm INT}$ versus loading increments. Panel (b) shows the integrated stress $\sigma_{xx}^{\rm INT}$ versus loading increments for a portion of the full model. Panel (b) shows the final strain localization pattern for all three simulations.

5.3.1 Interseismic period and stress drops

Figure ?? illustrates the displacement increments Δu_x during the interseismic period (Figures ??a-b) and the stress drops (Figures ??c-d). For instance, Figure ??a shows the displacement increment $\Delta u_x = u_x(t_3) - u_x(t_2)$, where $u_x(t_2)$ and $u_x(t_3)$ represent the displacement fields at the beginning and end of the interseismic period, respectively (the period between two high-amplitude stress drops. Similarly, the displacement increments $\Delta u_x = u_x(t_2) - u_x(t_1)$ during major stress drops are shown in Figures ??c-d. It is evident that displacement accumulates during the interseismic period (without major stress drops) and also intensifies during major stress drops.

Our simulation results also demonstrate the material's behavior during interseismic periods, where displacement gradually accumulates without significant stress drops. As shown in Figure $\bf ??$, displacement increments Δu_x during interseismic periods increase progressively as loading continues. This behavior mirrors the slow, ascismic slip observed between seismic events in fault zones. The gradual buildup of displacement during interseismic periods reflects the loading of the fault system, while the rapid displacement during stress drops corresponds to seismic slip. However, our model does not explicitly establish a causal link between ascismic slip accumulation and subsequent stress drops, which requires further investigation.

These findings suggest that the interaction between elastic and plastic deformation plays a critical role in controlling the timing and magnitude of seismic events. The gradual accumulation of displacement during the interseismic period reflects the fault's capacity to store elastic strain energy, which is then rapidly released during seismic events, leading to a stress drop.



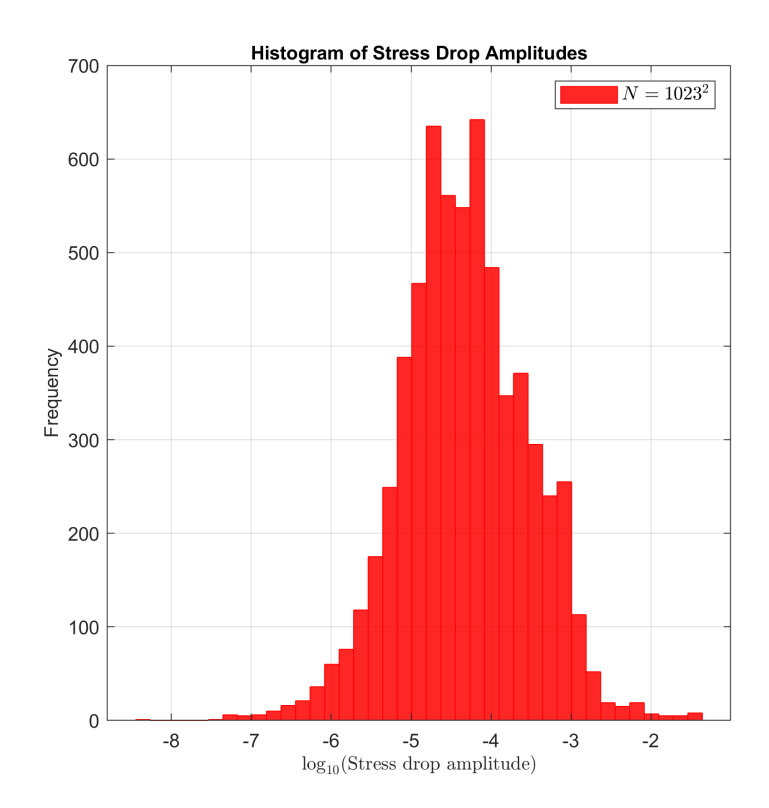


Figure 9. Histogram of of stress drop amplitudes for different resolutions. Panel (computed from a) shows the integrated stress $\sigma_{xx}^{\rm INT}$ versus loading increments. Panel high-resolution simulation (b $N=1023^2$) shows the histogram. The amplitude of stress-each drop amplitudes for three different resolutions. Panel (c) shows is defined as the histogram of difference in integrated axial stress drop amplitudes for two different resolutions between consecutive local maxima and minima, and plotted on a base-10 logarithmic scale. Panel (d) shows the histogram The resulting distribution is non-Gaussian and asymmetric, spanning over five orders of magnitude, with frequent small drops and rarer large-scale stress drop amplitudes for four different resolutions releases—consistent with turbulence-like plastic deformation dynamics.

Gutenberg-Richter-like law, which describes the frequency-magnitude distribution of earthquakes; however, a more detailed analysis is required to establish a direct connection, particularly from a plastic deformation perspective prevalence of small events and the presence of occasional larger ones are qualitatively consistent with the Gutenberg-Richter relationship. However, we emphasize that our current study does not perform a statistical fit (e.g., power-law or log-normal) to extract quantitative scaling exponents. Such an analysis would be required to firmly establish the statistical nature of the tail and its connection to real seismicity. Overall, the histogram of stress drop amplitudes reinforces supports the idea that the simplest even minimal elasto-plastic models, despite their minimalistic assumptions, are capable of capturing complex, emergent behavior that is often associated with more sophisticated models of seismicity with no prescribed faults or complex frictional laws, can give rise to rich and realistic emergent behavior.

445

450

5.3.2 Wave propagation due to a single stress drop

465

5.3.3 Earthquake triggering due to a single stress drop

Figure 10 displays the integrated stress σ^{INT}_{xx} versus loading increments and the wave fields (velocity Figure 10 shows the snapshots of wave fields following a single stress drop. The wave response is visualized in terms of velocity (v_x and pressure) and pressure (p) at the initial stage (Figures 10a-b) and after 250 different physical time steps(Figures 10e-d). The initial wavefield pattern is complex mostly corresponds to nucleation is shear (i.e., as Panels (a) and (b) present the initial wavefield immediately after the stress drop. The velocity and pressure distributions are spatially complex and dominated by shear-dominated nucleation patterns, qualitatively resembling a double-couple mechanism) and in a the volumetric component (pressure). The velocity field exhibits high amplitudes amplitudes, indicating simultaneous compressional response.

Panels (c)–(Figures 10b and 10d), indicating that the shear component has high amplitudes. (e)–(f), and (g)–(h) show the evolution of the wavefield after 360, 720, and 1080 time steps, respectively. The velocity field, initially concentrated near the nucleation region, spreads outward as the system relaxes dynamically. The pressure field also evolves, exhibiting outward-propagating features that reflect the elastic response of the medium. These results indicate that a localized stress drop in a plastic medium generates complex wave activity, with both velocity and pressure fluctuations contributing to the redistribution of energy. The simulation is performed with a time step size of $\Delta t = 4 \times 10^{-5}$.

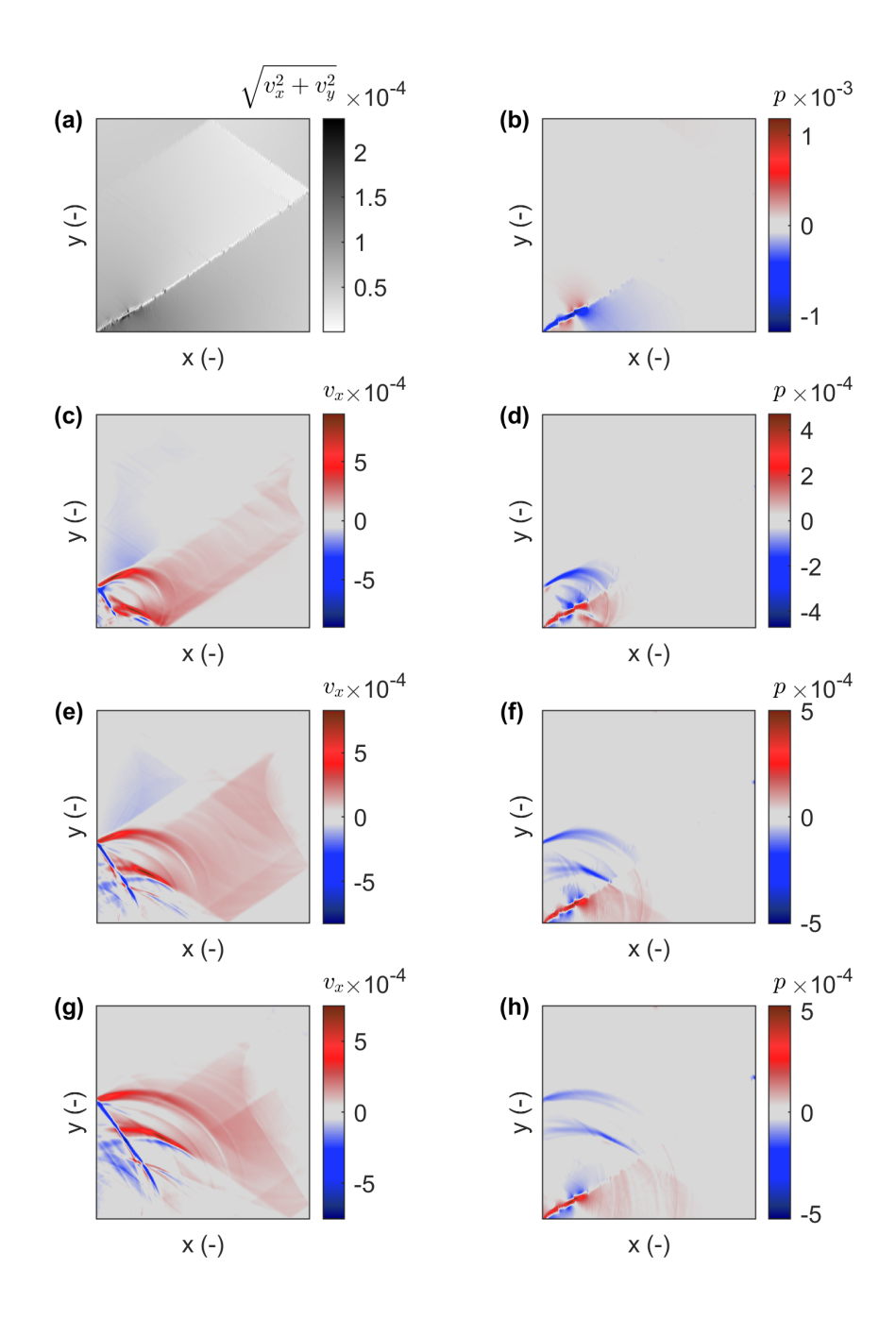


Figure 10. Earthquake nucleation due to Wave propagation following a single stress drop. Panels (a-ba-b) show the wave fields initial wavefields: (a) velocity v_x magnitude $\sqrt{v_x^2 + v_y^2}$, and pressure p(b) at the initial stagepressure p. Panels (e-dc-d)show the wave fields, (velocity v_x and pressure p(c) fields after 500-360, 720, and 1080 physical time steps, respectively. Panels—The pattern indicates nucleation dominated by shear (e-ddouble-couple-like) show the wave fields (velocity v_x and volumetric pressure p) after 750 time steps release, consistent with the early stages of dynamic rupture.

6 Discussion

475

480

485

490

495

500

470 **6.1** The nature of stress drops

As can be seen in Figure 8, during the loading, many shown in Figure 8, numerous stress drops occur throughout the loading process. From a theoretical perspective, the first stress dropafter standpoint, the initial stress drop—following the onset of strain localizationwas predicted and—has been analyzed by, e.g., Vermeer (1990) and Le Pourhiet (2013). The following stress drops occur due to switches for example, Vermeer (1990) and Le Pourhiet (2013). Subsequent stress drops are associated with transitions between quasi-static loading intervals. These stress drops correspond to transitions where the system moves from one quasi-static equilibrium events represent moments when the system shifts from one quasi-equilibrium state to another due to the inability of strain localization to continue growing in the prescribed direction. Once the breakdown of stable deformation paths. Specifically, when local stresses exceed the yield eriteriacriterion, plastic deformation is activated, causing a redistribution of stresses and, consequently, a rapid drop in stress. stress and a rapid release of stored energy in the form of a stress drop.

This process mimics the mechanics of fault rupture, where the accumulation of strain energy leads to a sudden release in the form of an earthquake.

The observed stress drops are consistent with those expected in elasto-plastic materials, where plastic yielding results in rapid shifts in the stress state. In our simulations, these stress drops are sharp and distinct, especially at higher temporal and spatial resolutions. This behaviorreflects the real-world phenomenon of earthquake triggering, where a sudden stress drop corresponds to a seismic event nucleation. accumulated strain energy is suddenly released during seismic events. The sharp, discrete stress drops observed in our simulations—particularly at high spatial and temporal resolutions—are consistent with such rupture-like behavior.

In addition to stress drop magnitudesBeyond the magnitude of individual stress drops, the spatial patterns distribution of strain localization play a critical role in determining the nature of stress release. In particular, localized shear bands act as conduits plays a key role in governing how stress is released. Localized shear bands serve as preferential paths for stress concentration, dietating how and where stress is released and redistribution, determining the geometry and timing of stress release. The interplay between elastic loading during the interseismic period and interseismic intervals and localized plastic deformation during stress drops provides a simplified but effective model for capturing earthquake cyclesoffers a minimal yet effective model of the earthquake cycle.

6.2 Role of regularization in elasto-plastic simulations

Regularization is crucial plays a critical role in numerical simulations of elasto-plastic materials, particularly in models involving strain localization especially when strain localization is involved. Without regularization, simulations can exhibit unrealistic results, such as the formation of may produce unphysical results such as infinitely narrow shear bands. In our and grid-dependent failure modes. In this study, the regularization parameter η^{vp} was carefully chosen to prevent such

artifacts while preserving the physical realism of the viscoplastic regularization parameter η^{vp} was carefully selected to ensure numerical stability while preserving physically realistic stress and strain fields.

The absence of regularizationcan lead to numerically unstable results, where stress drops occur too frequently or are too abrupt, producing non-physical behaviors in the model. On the other hand, excessive regularization Excessive regularization, however, can overly smooth out stress and strain these fields, suppressing the formation of localized shear bands and strain localization and significantly reducing the occurrence and sharpness of stress drops. The balance between these extremes is key to accurately modeling the dynamic behavior of elasto-plastic systems. This effect is clearly observed in low-resolution simulations, where the regularization length scale becomes comparable to or larger than the grid resolution. Conversely, insufficient regularization can result in non-convergent or unstable solutions.

Our results demonstrate that appropriate regularization is necessary enables the model to capture both the broad large-scale and fine-scale features of earthquake triggering, such as the spatial distribution of strain localization dynamic deformation—specifically, the spatial organization of shear bands and the timing and magnitude of stress drops. The These findings align with prior studies that show work emphasizing the importance of regularization in stabilizing numerical simulations of plastic elasto-plastic modeling, particularly for resolving localized deformation while maintaining physical accuracy convergence and computational stability (Popov and Sobolev, 2008; Duretz et al., 2018).

6.3 3D simulations with zero regularization

505

510

515

520

525

530

Alkhimenkov et al. (2023) performed 3D Alkhimenkov et al. (2023) conducted three-dimensional simulations of a single-phase elasto-plastic model with zero without regularization. These simulations provide valuable insights results provide valuable insight into how strain localization and stress drops manifest in fully 3D domains. The tests performed three-dimensional domains. Notably, the trends observed in 3D, both in temporal and spatial resolutions, show similar trends with the results of the both in terms of spatial and temporal resolution—are consistent with the 2D simulations results presented in this study.

The extension to 3D is important because it allows Extending the analysis to three dimensions is essential for a more realistic representation of fault systems, which are inherently three-dimensional in nature. In 3D, the stress and strain fields exhibit more complex behaviors, such as the formation of multiple interacting shear bandsor additional complexity, including the development of intersecting or branching shear bands, and the influence of out-of-plane stresses on fault sliprupture propagation. The fact that the unregularized 3D simulations without regularization produced results consistent with our 2D study underscores produce physically meaningful and qualitatively similar results further validates the robustness of the elastoplastic model used in this research framework employed here. This also suggests that certain dynamic features—such as stress drop sequences and fault-like deformation—can emerge naturally in elasto-plastic systems even in the absence of artificial smoothing.

6.4 Implications for earthquake triggering sequences and fault mechanics

The results from of both 2D and 3D simulations provide important implications for our understanding of earthquake triggering (Alkhimenkov et al., 2023) simulations offer important insights into earthquake nucleation and fault mechanics. The stress

drops observed in our models are <u>directly</u> analogous to the rapid release of accumulated stress during <u>natural</u> seismic events, <u>suggesting that supporting the idea that pressure-sensitive</u> elasto-plastic models can <u>effectively capture the mechanics replicate</u> key features of rupture initiation. The <u>periodic nature quasi-periodic pattern</u> of stress drops, <u>interspersed with slower periods</u> of <u>separated by intervals of gradual</u> strain accumulation, mirrors the <u>earthquake-like cycleseen in nature</u>. As the <u>simulation progresses</u>, fundamental structure of the <u>seismic cycle</u>.

As deformation progresses, the emergence of multiple shear bands develop, and stress drops can occur repeatedly on the same shear band, rather than always initiating on new segments becomes evident. Importantly, stress drops do not always occur on newly formed bands—instead, they frequently reoccur along existing localized zones of weakness. This behavior elosely resembles natural faulting processes, where strain localization leads to repeated cycles is consistent with observations of natural fault systems, where pre-existing fault planes accommodate repeated episodes of stress accumulation and release along pre-existing fault structures over multiple cycles. Our results highlight the capacity of simple elasto-plastic models to reproduce not only the mechanical ingredients of rupture, but also the spatial memory and cyclic behavior observed in fault systems.

6.5 Comparison to rate-and-state friction models

535

540

545

550

555

560

While our this study focuses on elasto-plasticity as the primary mechanism driving governing stress drops and strain localization, it is important to consider how these results compare instructive to compare our approach to traditional rate-and-state friction (RSF) models. RSF models. Rate-and-state friction models have been successful in explaining many aspects of earthquake nucleation and widely used to describe fault slip behavior, particularly through due to their ability to capture velocity weakening and strengthening behaviors velocity-weakening and velocity-strengthening effects that are critical for earthquake nucleation and stability analyses.

In contrast, the elasto-plastic model used in this study presented here does not rely on any velocity-dependent friction laws but instead captures stress drops through plastic yieldingconstitutive law. Instead, stress drops emerge naturally through local plastic yielding when the material reaches a yield criterion. This distinction is important because it provides an alternative explanation for how faults might weaken and slip during seismic events. The fact that our elasto-plastic model produces stress drops without needing to invoke velocity weakening suggests that plastic deformation alone may be sufficient to explain certain aspects of fault slip behaviors ignificant: it suggests that fault weakening and slip can be modeled purely through stress-based plasticity, without invoking empirical velocity dependence.

Furthermore, classical RSF models typically describe fault slip on a predefined, spatially fixed fault interface. In our model, by contrast, faults emerge spontaneously as localized zones of plastic strain, allowing for the generation, reactivation, and migration of shear bands. This feature provides an important advantage in capturing fault system evolution in heterogeneous or evolving tectonic environments, which cannot be represented by single-fault RSF frameworks.

6.6 Limitations and future work

565

570

580

585

While our study provides the present study offers valuable insights into the mechanics of stress drops and strain localization, it is important to acknowledge the limitations of the current model. fault-like behavior in elasto-plastic materials, several limitations remain.

First, the model assumes homogeneous material properties, which may oversimplify the complexity of real fault zones. In reality, natural fault zones are highly heterogeneous, with variations in material properties that can significantly influence fault behavior lithology, porosity, cohesion, and pre-existing damage that significantly affect strain localization and rupture dynamics. Incorporating spatially variable properties would allow for a more realistic simulation of fault behavior and could reveal additional mechanisms of rupture complexity.

Additionally, the current model does not account for Second, the model currently neglects fluid-rock interactions, which.

Fluids are known to play a significant critical role in fault weakeningand earthquake triggering, particularly in fluid-saturated fault zones. Future work could extend this model to include poroelastic effects or fluid migration, which would provide a more complete picture of the processes governing fault slip, particularly through pore pressure buildup and fluid-induced instabilities.

Future extensions of this model should incorporate poroelasticity or two-phase flow to study the coupling between deformation and fluid transport, especially in overpressured or fluid-saturated fault zones.

Finally, while our results are based on the present study includes detailed two-dimensional simulations, the primary findings are limited to 2D simulations, future studies should further explore geometries. Three-dimensional simulations provide a more realistic framework for fault mechanics, capturing effects such as off-plane deformation, complex rupture geometries, and interactions among multiple shear bands. Alkhimenkov et al. (2023) performed 3D simulations, which are more representative of real fault systems. Extending the present model to include of elasto-plastic deformation and observed multiple stress drops consistent with the results presented here. However, that study did not focus on earthquake nucleation or the dynamics of earthquake sequences. Future high-resolution 3D geometries, along with higher-resolution simulations, would allow for a more detailed investigation of fault mechanics and earthquake triggeringstudies will be essential for advancing elasto-plastic modeling of seismic processes, particularly in relation to rupture initiation, stress transfer, and fault interaction in realistic geological settings.

590 7 Conclusions

595

610

615

620

In this study, we investigated stress drops and earthquake triggering earthquake-like behavior in idealized elasto-plastic media through using two-dimensional numerical simulations. The first stress drop develops after occurs following the onset of strain localization due to a process driven by structural softening (Vermeer, 1990; Le Pourhiet, 2013; Sabet and de Borst, 2019). The following stress drops occur due to switches Subsequent stress drops are associated with transitions between quasi-static loading intervals. These stress drops correspond to transitions, where the system moves from one quasi-static equilibrium equilibrium state to another due to the inability of strain localization to continue growing in the prescribed direction. The structural softening phenomenon received This structural softening mechanism, which received relatively little attention until recently (Sabet and de Borst, 2019) and studied, is explored here as a mechanism fundamental driver of sudden stress drops and potential triggering of earthquakes release and potential earthquake nucleation.

Our results underscore the critical role importance of both temporal and spatial resolutions resolution in capturing the evolution of stress and strain fields during seismic cycles. The convergence tests demonstrated that finer temporal discretization sharpens the observed throughout the seismic cycle. Convergence tests demonstrate that finer discretization sharpens stress drops and leads to lower minimum stress values, underscoring the importance of accurately resolving emphasizing the need for high-resolution modeling to accurately resolve dynamic stress changes. Similarly, spatial resolution tests showed that while broad patterns of accumulated strain were consistent across different resolutions, higher-resolution grids provided significantly more detail, capturing intricate strain localization and stress redistribution mechanisms that are essential for modeling realistic earthquake behavior.

The analysis of Analysis of the interseismic periods and stress drops revealed that displacement gradually accumulates during the interseismic phase, followed by intensified strain during major stress drops. This behavior reveals a typical cycle: gradual displacement accumulation followed by abrupt, localized deformation. This mirrors the natural earthquake cycle, where periods of slow, in which periods of aseismic slip are followed by rapid, seismic slip interrupted by rapid seismic events that release accumulated strain energy. Furthermore, our detailed investigation of earthquake nucleation due to Moreover, wavefield analysis following a single stress drop revealed complex initial wave field patterns, with high-amplitude shear components dominating the response, providing insights nucleation patterns, offering insight into the mechanics of rupture initiation.

One of the key contributions of this study work is the demonstration that simple pressure-sensitive elasto-plastic models with constant friction coefficient in time and spacefriction coefficient, when coupled with high-resolution discretizations, are capable of reproducing—can reproduce key features of earthquake triggering sequences and stress drop behavior, without relying on more provided sufficient spatial and temporal resolution. Notably, this is achieved without the use of complex frictional laws or velocity-dependent weakening mechanisms. This indicates Our results show that plastic yielding alone can account for some of the fundamental processes governing fundamental aspects of fault slip and rupture. A second important contribution is that faults are not prescribed a priori, as in conventional rate-and-state models; instead, new faults emerge spontaneously from the evolving stress field, offering a key advantage in modeling complex fault dynamics.

Our findings have several These findings have important implications for seismic hazard assessment and the development of predictive models. First, they emphasize the necessity of incorporating highlight the need for high-resolution spatial and temporal discretizations into numerical models to accurately capture the localized and transient capture the transient, localized phenomena that govern earthquake triggering. Second, the results confirm previous studies highlighting the important they reaffirm the critical role of plastic deformation in fault weakening and rupture, suggesting that plasticity should be considered incorporated alongside traditional frictional models in future earthquake simulations.

Finally, while our study has focused formulations in future modeling efforts. Finally, although this study focuses on two-dimensional idealized elasto-plastic mediasettings, the insights gained here provide a solid provide a foundation for extending the analysis to more complex, framework to more realistic three-dimensional fault systems and heterogeneous materials, heterogeneous systems. Future research could explore the interactions interaction between plasticity, material heterogeneity, and fluid migration, providing thereby contributing to a more comprehensive understanding of the mechanics physical mechanisms underlying seismic events. By advancing these models, we move Advancing these models brings us closer to developing more accurate robust, physics-based tools for predicting earthquake behavior and mitigating seismic risk earthquake forecasting and seismic risk mitigation.

Code availability

625

630

635

The software developed and used in the scope of this study is licensed under MIT License. The latest versions of the code is available from a permanent DOI repository (Zenodo) at: https://doi.org/10.5281/zenodo.15035487-.16412530 (last access: 16 March 24 July 2025) (Alkhimenkov et al., 2025a)(Alkhimenkov et al., 2025b). The repository contains code examples and can be readily used to reproduce the figures of the paper. The codes are written using the Matlab, and CUDA C programming languages. Refer to the repositories' README for additional information.

Author contribution

YA designed the original study, developed the codes and algorithms, performed benchmarks, created the figures, and wrote the manuscript. LK contributed to the study design, helped develop the codes and algorithms, and edited the manuscript. YP provided early work on accelerated PT methods, contributed to the study design, helped develop the codes and algorithms, assisted with the interpretation of the results, edited the manuscript, and supervised the work.

Competing interests

The contact author has declared that none of the authors has any competing interests.

650 Financial support

Yury Alkhimenkov gratefully acknowledges support from the Swiss National Science Foundation, project number P500PN_206722. Lyudmila Khakimova and Yury Podladchikov thank the Russian Science Foundation (project №24-77-10022) for supporting the development of numerical algorithms and facilitating large-scale GPU-based computations.

References

665

- Alkhimenkov, Y. and Podladchikov, Y. Y.: Accelerated pseudo-transient method for elastic, viscoelastic, and coupled hydromechanical problems with applications, Geoscientific Model Development, 18, 563–583, https://doi.org/10.5194/gmd-18-563-2025, 2025.
 - Alkhimenkov, Y., Räss, L., Khakimova, L., Quintal, B., and Podladchikov, Y.: Resolving wave propagation in anisotropic poroelastic media using graphical processing units (GPUs), Journal of Geophysical Research: Solid Earth, 126, e2020JB021 175, 2021.
- Alkhimenkov, Y., Khakimova, L., Utkin, I., and Podladchikov, Y.: Resolving Strain Localization of Brittle and Ductile Deformation in two-and three-dimensions using Graphical Processing Units (GPUs), arXiv preprint arXiv:2305.01701, 2023.
 - Alkhimenkov, Y., Khakimova, L., and Podladchikov, Y.: Shear bands triggered by solitary porosity waves in deforming fluid-saturated porous media, Geophysical Research Letters, 51, e2024GL108 789, 2024a.
 - Alkhimenkov, Y., Khakimova, L., Utkin, I., and Podladchikov, Y.: Resolving strain localization in frictional and time-dependent plasticity: Two-and three-dimensional numerical modeling study using graphical processing units (GPUs), Journal of Geophysical Research: Solid Earth, 129, e2023JB028 566, 2024b.
 - Alkhimenkov, Y., Khakimova, L., and Podladchikov, Y.: FastLocalization_2D_Stress_Drops, https://doi.org/10.5281/zenodo.15035487, 2025a.
 - Alkhimenkov, Y., Khakimova, L., and Podladchikov, Y.: FastLocalization_2D_Stress_Drops, https://doi.org/10.5281/zenodo.16412530, 2025b.
- Allison, K. L. and Dunham, E. M.: Earthquake cycle simulations with rate-and-state friction and power-law viscoelasticity, Tectonophysics, 733, 232–256, 2018.
 - Andrews, D.: Rupture propagation with finite stress in antiplane strain, Journal of Geophysical Research, 81, 3575–3582, 1976.
 - Andrews, D.: Rupture dynamics with energy loss outside the slip zone, Journal of Geophysical Research: Solid Earth, 110, 2005.
 - Byerlee, J. and Savage, J. C.: Coulomb plasticity within the fault zone, Geophysical Research Letters, 19, 2341–2344, 1992.
- 675 Cundall, P.: Numerical experiments on localization in frictional materials, Ingenieur-archiv, 59, 148–159, 1989.
 - Cundall, P.: Numerical modelling of jointed and faulted rock, in: International conference on mechanics of jointed and faulted rock, pp. 11–18, 1990.
 - Dal Zilio, L., Lapusta, N., Avouac, J.-P., and Gerya, T.: Subduction earthquake sequences in a non-linear visco-elasto-plastic megathrust, Geophysical Journal International, 229, 1098–1121, 2022.
- de Borst, R. and Duretz, T.: On viscoplastic regularisation of strain-softening rocks and soils, International Journal for Numerical and Analytical Methods in Geomechanics, 44, 890–903, 2020.
 - De Borst, R., Crisfield, M. A., Remmers, J. J., and Verhoosel, C. V.: Nonlinear finite element analysis of solids and structures, John Wiley & Sons, 2012.
 - de Souza Neto, E. A., Peric, D., and Owen, D. R.: Computational methods for plasticity: theory and applications, John Wiley & Sons, 2011.
- Dieterich, J. H.: Time-dependent friction and the mechanics of stick-slip, Rock friction and earthquake prediction, pp. 790–806, 1978.
 - Dieterich, J. H.: Modeling of rock friction: 1. Experimental results and constitutive equations, Journal of Geophysical Research: Solid Earth, 84, 2161–2168, 1979.
 - Dormy, E. and Tarantola, A.: Numerical simulation of elastic wave propagation using a finite volume method, Journal of Geophysical Research: Solid Earth, 100, 2123–2133, 1995.
- 690 Drucker, D. C. and Prager, W.: Soil mechanics and plastic analysis or limit design, Quarterly of applied mathematics, 10, 157–165, 1952.

- Duretz, T., Souche, A., De Borst, R., and Le Pourhiet, L.: The benefits of using a consistent tangent operator for viscoelastoplastic computations in geodynamics, Geochemistry, Geophysics, Geosystems, 19, 4904–4924, 2018.
- Duretz, T., de Borst, R., and Le Pourhiet, L.: Finite thickness of shear bands in frictional viscoplasticity and implications for lithosphere dynamics, Geochemistry, Geophysics, Geosystems, 20, 5598–5616, 2019.
- Duretz, T., de Borst, R., and Yamato, P.: Modeling lithospheric deformation using a compressible visco-elasto-viscoplastic rheology and the effective viscosity approach, Geochemistry, Geophysics, Geosystems, 22, e2021GC009 675, 2021.
 - Erickson, B. A., Dunham, E. M., and Khosravifar, A.: A finite difference method for off-fault plasticity throughout the earthquake cycle, Journal of the Mechanics and Physics of Solids, 109, 50–77, 2017.
 - Frankel, S. P.: Convergence rates of iterative treatments of partial differential equations, Mathematics of Computation, 4, 65–75, 1950.
- Gabriel, A.-A., Ampuero, J.-P., Dalguer, L., and Mai, P. M.: Source properties of dynamic rupture pulses with off-fault plasticity, Journal of Geophysical Research: Solid Earth, 118, 4117–4126, 2013.
 - Heeres, O. M., Suiker, A. S., and de Borst, R.: A comparison between the Perzyna viscoplastic model and the consistency viscoplastic model, European Journal of Mechanics-A/Solids, 21, 1–12, 2002.
- Johnson, P. A., Savage, H., Knuth, M., Gomberg, J., and Marone, C.: Effects of acoustic waves on stick–slip in granular media and implications for earthquakes, Nature, 451, 57–60, 2008.
 - Kaneko, Y. and Fialko, Y.: Shallow slip deficit due to large strike-slip earthquakes in dynamic rupture simulations with elasto-plastic off-fault response, Geophysical Journal International, 186, 1389–1403, 2011.
 - Lavier, L. L., Roger Buck, W., and Poliakov, A. N.: Self-consistent rolling-hinge model for the evolution of large-offset low-angle normal faults, Geology, 27, 1127–1130, 1999.
- 710 Le Pourhiet, L.: Strain localization due to structural softening during pressure sensitive rate independent yielding, Bulletin de la Société géologique de France, 184, 357–371, 2013.
 - Lemiale, V., Mühlhaus, H.-B., Moresi, L., and Stafford, J.: Shear banding analysis of plastic models formulated for incompressible viscous flows, Physics of the Earth and Planetary Interiors, 171, 177–186, 2008.
- Ma, S.: A physical model for widespread near-surface and fault zone damage induced by earthquakes, Geochemistry, Geophysics, Geosystems, 9, 2008.
 - Ma, S. and Andrews, D.: Inelastic off-fault response and three-dimensional dynamics of earthquake rupture on a strike-slip fault, Journal of Geophysical Research: Solid Earth, 115, 2010.
 - Moresi, L., Mühlhaus, H.-B., Lemiale, V., and May, D.: Incompressible viscous formulations for deformation and yielding of the lithosphere, Geological Society, London, Special Publications, 282, 457–472, 2007.
- Poliakov, A. and Herrmann, H.: Self-organized criticality of plastic shear bands in rocks, Geophysical Research Letters, 21, 2143–2146, 1994.
 - Poliakov, A., Podladchikov, Y., and Talbot, C.: Initiation of salt diapirs with frictional overburdens: numerical experiments, Tectonophysics, 228, 199–210, 1993.
 - Poliakov, A. N., Herrmann, H. J., Podladchikov, Y. Y., and Roux, S.: Fractal plastic shear bands, Fractals, 2, 567–581, 1994.
- Popov, A. and Sobolev, S. V.: SLIM3D: A tool for three-dimensional thermomechanical modeling of lithospheric deformation with elasto-visco-plastic rheology, Physics of the earth and planetary interiors, 171, 55–75, 2008.
 - Pranger, C., Sanan, P., May, D. A., Le Pourhiet, L., and Gabriel, A.-A.: Rate and state friction as a spatially regularized transient viscous flow law, Journal of Geophysical Research: Solid Earth, 127, e2021JB023 511, 2022.

- Preuss, S., Ampuero, J. P., Gerya, T., and van Dinther, Y.: Characteristics of earthquake ruptures and dynamic off-fault deformation on propagating faults, Solid Earth Discussions, 2020, 1–39, 2020.
 - Räss, L., Utkin, I., Duretz, T., Omlin, S., and Podladchikov, Y. Y.: Assessing the robustness and scalability of the accelerated pseudo-transient method, Geoscientific Model Development, 15, 5757–5786, 2022.
 - Ruina, A.: Slip instability and state variable friction laws, Journal of Geophysical Research: Solid Earth, 88, 10359-10370, 1983.
- Sabet, S. A. and de Borst, R.: Structural softening, mesh dependence, and regularisation in non-associated plastic flow, International Journal for Numerical and Analytical Methods in Geomechanics, 43, 2170–2183, 2019.
 - Scuderi, M., Marone, C., Tinti, E., Di Stefano, G., and Collettini, C.: Precursory changes in seismic velocity for the spectrum of earthquake failure modes, Nature geoscience, 9, 695–700, 2016.
 - Simpson, G.: Emergence and growth of faults during earthquakes: Insights from a dynamic elasto-plastic continuum model, Tectonophysics, 868, 230 089, 2023.
- Templeton, E. L. and Rice, J. R.: Off-fault plasticity and earthquake rupture dynamics: 1. Dry materials or neglect of fluid pressure changes, Journal of Geophysical Research: Solid Earth, 113, 2008.
 - Tong, X. and Lavier, L. L.: Simulation of slip transients and earthquakes in finite thickness shear zones with a plastic formulation, Nature communications, 9, 3893, 2018.
- Uphoff, C., May, D. A., and Gabriel, A.-A.: A discontinuous Galerkin method for sequences of earthquakes and aseismic slip on multiple faults using unstructured curvilinear grids. Geophysical Journal International, 233, 586–626, 2023.
 - Vermeer, P.: The orientation of shear bands in biaxial tests, Géotechnique, 40, 223–236, 1990.

750

- Virieux, J.: P-SV wave propagation in heterogeneous media: Velocity-stress finite-difference method, Geophysics, 51, 889-901, 1986.
- Wollherr, S., Gabriel, A.-A., and Uphoff, C.: Off-fault plasticity in three-dimensional dynamic rupture simulations using a modal Discontinuous Galerkin method on unstructured meshes: implementation, verification and application, Geophysical Journal International, 214, 1556–1584, 2018.
- Zienkiewicz, O. C. and Taylor, R. L.: The finite element method for solid and structural mechanics, Elsevier, 2005.